

Research Articles: Neurobiology of Disease

Disruption of endosomal sorting in Schwann cells leads to defective myelination and endosomal abnormalities observed in Charcot-Marie-Tooth disease

<https://doi.org/10.1523/JNEUROSCI.2481-21.2022>

Cite as: J. Neurosci 2022; 10.1523/JNEUROSCI.2481-21.2022

Received: 16 December 2021

Revised: 24 April 2022

Accepted: 3 May 2022

This Early Release article has been peer-reviewed and accepted, but has not been through the composition and copyediting processes. The final version may differ slightly in style or formatting and will contain links to any extended data.

Alerts: Sign up at www.jneurosci.org/alerts to receive customized email alerts when the fully formatted version of this article is published.

1 **Disruption of endosomal sorting in Schwann cells leads to defective myelination**
2 **and endosomal abnormalities observed in Charcot-Marie-Tooth disease**

3 John W. McLean¹, Julie A. Wilson¹, Tina Tian¹, Jennifer A. Watson¹, Mary VanHart¹,
4 Andrew J. Bean³, Steven S. Scherer⁴, David K. Crossman⁵, Eroboghene E. Ubogu^{1,2}
5 and Scott M. Wilson^{1,6}

6
7 ¹Department of Neurobiology, Evelyn F. McKnight Brain Institute, Civitan International
8 Research Center, University of Alabama at Birmingham, Birmingham, Alabama, 35294,
9 United States of America.

10 ²Division of Neuromuscular Disease, Department of Neurology, University of Alabama
11 at Birmingham, Birmingham, Alabama, 35294, United States of America

12 ³Rush University, Graduate College, Chicago, IL, 60612, United States of America.

13 ⁴Department of Neurology, Perelman School of Medicine at the University of
14 Pennsylvania, Philadelphia, Pennsylvania, 19104, United States of America

15 ⁵Department of Genetics, University of Alabama at Birmingham, Birmingham, Alabama,
16 35294, United States of America.

17 ⁶Submitting and Corresponding author. Email address: livvy01@uab.edu, phone (205)
18 975-5573, fax: (205) 934-6571. Postal Address: 1825 University Blvd, SHEL 914,
19 Birmingham, AL 35294, United States of America.

20

21 Number of pages: 48

22 Number of figures: 9

23

24 Number of words:

25 Abstract: 234

26 Introduction: 711

27 Discussion: 1165

28 Conflict of interest: The authors declare no competing financial interests

29 Acknowledgements: This research was supported by the University of Alabama at

30 Birmingham Department of Neurobiology and NIH–National Institute of Neurological

31 Disorders and Stroke Grant NS110744 to S.M.W. We thank Edward Phillips at the UAB

32 Electron Microscopy Core for help with tissue processing and collection of sciatic nerve

33 micrographs.

34

35

36 **Abstract**

37 Endosomal sorting plays a fundamental role in directing neural development. By
38 altering the temporal and spatial distribution of membrane receptors, endosomes
39 regulate signaling pathways that control the differentiation and function of neural cells.
40 Several genes linked to inherited demyelinating peripheral neuropathies, known as
41 Charcot-Marie-Tooth disease (CMT), encode proteins that directly interact with
42 components of the endosomal sorting complex required for transport (ESCRT). Our
43 previous studies demonstrated that a point mutation in the ESCRT component
44 hepatocyte growth factor-regulated tyrosine kinase substrate (HGS), an endosomal
45 scaffolding protein that identifies internalized cargo to be sorted by the endosome,
46 causes a peripheral neuropathy in the neurodevelopmentally-impaired *teetering* mice.
47 Here, we constructed a Schwann cell-specific deletion of *Hgs* to determine the role of
48 endosomal sorting during myelination. Inactivation of HGS in Schwann cells resulted in
49 motor and sensory deficits, slowed nerve conduction velocities, delayed myelination and
50 hypomyelinated axons, all of which occur in demyelinating forms of CMT. Consistent
51 with a delay in Schwann cell maturation, HGS-deficient sciatic nerves displayed
52 increased mRNA levels for several promyelinating genes and decreased mRNA levels
53 for genes that serve as markers of myelinating Schwann cells. Loss of HGS also altered
54 the abundance and activation of the ERBB2/3 receptors which are essential for
55 Schwann cell development. We therefore hypothesize that HGS plays a critical role in
56 endosomal sorting of the ERBB2/3 receptors during Schwann cell maturation, which
57 further implicates endosomal dysfunction in inherited peripheral neuropathies.

58

59 **Significance statement**

60 Schwann cells myelinate peripheral axons, and defects in Schwann cell function
61 cause inherited demyelinating peripheral neuropathies known as CMT. Although many
62 CMT-linked mutations are in genes that encode putative endosomal proteins, little is
63 known about the requirements of endosomal sorting during myelination. In this study,
64 we demonstrate that loss of HGS disrupts the endosomal sorting pathway in Schwann
65 cells, resulting in hypomyelination, aberrant myelin sheaths, and impairment of the
66 ERBB2/3 receptor pathway. These findings suggest that defective endosomal trafficking
67 of internalized cell surface receptors may be a common mechanism contributing to
68 demyelinating CMT.

69

70 **Introduction**

71 The endocytic pathway consists of a series of membrane trafficking steps that
72 regulate the internalization of cell-surface receptors and lipids (Jovic et al., 2010;
73 McNally and Cullen, 2018). Internalized cargo is initially delivered to early endosomes,
74 where it is sorted into distinct endocytic routes (Naslavsky and Caplan, 2018). From
75 here, internalized receptors can be recycled back to the cell surface through recycling
76 endosomes, continue to activate signaling pathways while residing on early endosomes,
77 or sorted to late endosomes, and subsequently to lysosomes, for degradation (Goh and
78 Sorkin, 2013; Cullen and Steinberg, 2018). By controlling the trafficking of internalized
79 cell surface receptors in this spatial and temporal manner, the endosomal pathway
80 regulates the composition, distribution and density of receptors at the cell surface as
81 well as the fate of signaling complexes within the cell (Redpath et al., 2020).

82 The ESCRT pathway aids in sequestering internalized cell surface cargo on the
83 endosome and determines how it is directed along the endolysosomal pathway (Hurley
84 and Emr, 2006; Hurley, 2008; Rusten et al., 2011). As part of the ESCRT complex, HGS
85 regulates the trafficking, degradation and recycling of a variety of cell surface receptors
86 (Hislop et al., 2004; Hanyaloglu et al., 2005; Yan et al., 2005; Huang et al., 2009;
87 Villasenor et al., 2016; Dauner et al., 2017; Haugen et al., 2017). The type of interaction
88 between components of the ESCRT pathway and the endosomal pathway influences
89 the fate of internalized cargo and, ultimately, how cells respond to external stimuli. For
90 instance, while HGS can downregulate the abundance of cell surface receptors by
91 sorting them to lysosomes (Bean et al., 2000; Raiborg et al., 2008; Belleudi et al.,
92 2009), it can also act as an endosomal scaffold that supports cell signaling (Huang et
93 al., 2009; Chanut-Delalande et al., 2010; Huang et al., 2010; Miura and Mishina,
94 2011b). However, little is known about how HGS and the endosomal pathway regulate
95 different signaling cascades in the context of the developing nervous system.
96 Numerous genes that encode proteins believed to regulate endocytic function have
97 been linked to demyelinating forms of CMT (Kalaydjieva et al., 2000; Hunter et al.,
98 2003; Street et al., 2003a; Bolis et al., 2007; Chow et al., 2007; Lupo et al., 2009; Horn
99 et al., 2012b; Sidiropoulos et al., 2012). Mutations in these genes have cell autonomous
100 effects in Schwann cells, resulting in defective formation or maintenance of myelin
101 sheaths (Barisic et al., 2008; Brennan et al., 2015). The endocytic deficits caused by
102 these mutations include defective endocytosis, inhibition of receptor recycling, and
103 impaired lysosomal sorting (Kachhap et al., 2007; Lupo et al., 2009; Lee et al., 2011;
104 Lee et al., 2012; Pietiainen et al., 2013). CMT-linked proteins have also been shown to

105 interact with components of the ESCRT pathway and play a role in their stability and
106 localization (Lee et al., 2012; Pietiainen et al., 2013; Li et al., 2015). For example,
107 mutations in Lipopolysaccharide-induced tumor necrosis factor (LITAF/SIMPLE) that are
108 linked to demyelinating CMT also reduce endosomal HGS levels (Street et al., 2003b;
109 Lee et al., 2012).

110 We previously showed that a point mutation in *Hgs* (*Hgs^{tn}*) causes defective
111 myelination (Watson et. al., 2015). Although mice that are heterozygous for the *Hgs^{tn}*
112 allele showed differences in tactile sensitivity and performance in a forced swim test
113 compared to control (Watson et. al., 2015, Meier, 1967), it is not known if the
114 myelination deficit caused by this allele is also inherited in a dominant manner. To
115 examine the cell autonomous effects of loss of HGS on peripheral nerve development,
116 we therefore generated a mouse line that specifically deleted *Hgs* in Schwann cells.
117 Loss of HGS resulted in abnormal myelin sheaths and caused severe motor and
118 sensory deficits similar to those observed in demyelinating CMT (Zoidl et al., 1995;
119 Erdem et al., 1998; Colby et al., 2000; Barisic et al., 2008; Pisciotta and Shy, 2018).
120 HGS-deficient Schwann cells were also hyperproliferative and expressed increased
121 levels of promyelinating genes. In addition to altering the abundance and activation of
122 the myelin-inducing ERBB2/3 receptor tyrosine kinases that traffic through the
123 endosomal pathway in Schwann cells, deletion of *Hgs* also altered the activation of the
124 downstream AKT kinase. These findings suggest a critical role for endosomal sorting of
125 the ERBB2/3 receptors during Schwann cell maturation and for peripheral nerve
126 myelination.

127

128 **Materials and Methods**129 **Animals**

130 Wild type C57BL/6J mice were originally obtained from Jackson Laboratories,
131 and *Hgs*-floxed mice (which we refer to as *Hgs^{fl}* mice) that contain the
132 *Hgs^{tm1a(EUCOMM)Wtsi}* allele of *Hgs* were obtained from Helmholtz Zentrum München -
133 German Research Center for Environmental Health (GmbH). *Hgs^{fl}* mice contain *loxP*
134 sites in the intronic sequences that flank exon 5 of the *Hgs* gene and were maintained
135 on a C57BL/6J background. These control *Hgs^{fl}* mice were indistinguishable from wild
136 type C57BL/6J mice. To delete exon 5 of the *Hgs* gene specifically in Schwann cells,
137 *Hgs^{fl}* mice were crossed to hemizygous *P0Cre* mice (B6N.FVB-Tg(*Mpz-Cre*)26Mes/J)
138 that were purchased from Jackson Laboratories (Stock number 017927). These *P0Cre*
139 transgenic mice express Cre recombinase under the control of the myelin protein zero
140 (*P₀*, *Mpz*) promoter as early as embryonic day 14 (Feltri et al., 1999b). As a result, exon
141 5 of the *Hgs* gene is specifically deleted in the Schwann cells of the resulting C57BL/6-
142 Tg(*Mpz-cre*)26Mes *Hgs^{tm1fl/fl}* mice (which we refer to as *P0CreHgs^{fl}* mice) that were
143 used in all subsequent experiments.

144 All mouse strains have been maintained in our breeding colony at the University
145 of Alabama at Birmingham, which is fully accredited by the Association for Assessment
146 and Accreditation of Laboratory Animal Care International (A3255-01). All efforts were
147 made to minimize animal suffering, and all research was performed in compliance with
148 the United States Animal Welfare Act and other federal statutes and regulations relating
149 to animals. Our studies adhered to the principles stated in the Guide for the Care and
150 Use of Laboratory Animals, United States National Research Council. In addition, all

151 experiments were carried out with the approval of the University of Alabama at
152 Birmingham's Institutional Animal Care and Use Committee (Protocol #21800). To
153 ensure that there was no gender bias, equal numbers of both female and male mice
154 were used in this study, and gender difference did not influence any of the reported
155 outcomes.

156 For genotyping mice, tail DNA was obtained by alkaline lysis extraction, and
157 polymerase chain reactions were performed using Mango Taq polymerase (Meridian
158 Biosciences, Cat# BIO-21083) according to the manufacturer's instructions. Mice were
159 genotyped for the *Hgs^{fl}* allele using forward primer 5' AAGGGGGACACA
160 CAAGCAAAA-3' and reverse primer 5'-CAGCTGAGACTGCTGTGACA-3', and the
161 presence of the *P0Cre* transgene was identified using forward primer 5'-
162 CCACCACCTCTCCATTGCAC-3' and reverse primer 5'-
163 ATGTTTAGCTGGCCCAAATG-3'. Thermocycling conditions were one cycle at 94°C for
164 2 min, 25 cycles at 94°C for 30 s, 58°C for 30 s and 72°C for 30 s, followed by a single
165 hold at 72°C for 7 min and then held at 4°C until resolution by agarose gel
166 electrophoresis.

167 **Body and muscle mass analysis**

168 Total body and gastrocnemius muscle masses were obtained from 1- and 4-
169 month-old *P0CreHgs^{fl}* mice and *Hgs^{fl}* controls. Masses were collected from at least 5
170 animals per genotype, with equal numbers of male and female mice used for each
171 genotype, and the values are reported as the average muscle or body mass \pm SEM.
172 Unpaired Student's t-tests were performed to determine statistical significance.

173

174 **Behavioral analysis**

175 Motor and sensory performance of *Hgs^{fl}* control mice and *POCreHgs^{fl}* mice were
176 evaluated at both 1 and 4 months of age from at least 5 animals per genotype, with
177 equal numbers of male and female mice used for each genotype. Mice were handled at
178 least two days prior to open field testing. Before each behavioral assay, mice were
179 allowed to habituate to the testing room for 30 min. On the test day, mice were placed in
180 the center of an open field arena (43 × 43 × 30 cm Plexiglas box), locomotion was
181 measured for 5 min by photo beam detectors, and recorded data was analyzed using
182 ENV-515 software (Med Associates).

183 Motor coordination and balance were assessed by placing mice on an
184 accelerating rotarod (ENV-575, Med Associates) and recording latency to fall. The
185 rotarod began rotating at 3.5 revolutions per minute (rpm) and accelerated to 35 rpm
186 over a 5 min period. Each mouse performed three trials a day, with a 15 min inter-trial
187 rest period, for three consecutive days. The presented latency to fall is the average of
188 the three daily averages for each mouse.

189 The Chatillon Ametek Force Gauge was used to assay forelimb grip strength,
190 and the maximum amount of force generated by the forelimbs was recorded. Each
191 mouse trial consisted of 12 repetitions of the assay with the two highest and two lowest
192 data points dropped from final analysis. Unpaired Student's t-tests were performed to
193 determine statistical significance.

194 To test tactile sensitivity, mice were assessed using the von Frey filaments test.
195 Animals were habituated to an open gridded floor chamber for 10 min. A series of 12
196 von Frey fibers ranging from 0.02 to 8 g of force (North Coast Medical) was applied from

197 below the mesh grid in ascending order beginning with the smallest fiber. Fiber
198 application was limited to the central region of the plantar surface to avoid the foot pads,
199 and the hind paw withdrawal threshold was determined. Unpaired Student's t-tests were
200 performed to determine statistical significance.

201 **Sciatic nerve morphology**

202 Sciatic nerves were dissected from *Hgs^{fl}* and *P0CreHgs^{fl}* mice, fixed in 3%
203 paraformaldehyde/2% glutaraldehyde in 0.2 M sodium cacodylate buffer for 1.5 h,
204 washed in 0.2 M sodium cacodylate, and then post-fixed in 1% osmium tetroxide for 1 h
205 in the dark. After thoroughly washing with 0.2 M sodium cacodylate, samples were
206 dehydrated in a graded acetone series of increasing concentration (50%, 75%, 90%,
207 95%, 100% x 4) for 10 min each step and infiltrated with epoxy resin (Electron
208 Microscopy Sciences) by rotating samples overnight in a 1:1 epoxy:acetone solution.
209 The following day, samples were rocked in fresh 100% epoxy for at least 3 x 2 h,
210 embedded, then polymerized in resin overnight at 65°C. Ultra-thin cross-sections were
211 collected using a Leica EM-UC6 ultramicrotome and stained for contrast with uranyl
212 acetate and lead citrate. Samples were viewed using an FEI Tecnai T-12 electron
213 microscope with a Hamamatsu digital camera.

214 Images for morphometric analysis were acquired from adjacent but non-
215 overlapping fields to measure large caliber axons (diameter > 1 micron), myelin
216 thickness, and axonal density. The g-ratio was calculated by dividing the axon diameter
217 by the axon + myelin diameter, and the relevant measurements were obtained with
218 ImageJ software (NIH). At least 106 axons were quantified across at least two separate
219 fields for each animal. Micrographs taken at 470x magnification were utilized to

220 measure the number of myelinated fibers, while micrographs taken at 1100x
221 magnification were used to determine g-ratios. The Kolmogorov-Smirnov test was used
222 to determine differences in the frequency of axon diameters.

223 **Protein Isolation**

224 Mice were deeply anesthetized with 5% isoflurane to minimize pain and distress
225 prior to rapid decapitation. Sciatic nerves and brains were dissected and homogenized
226 in modified RIPA buffer containing 50 mM Tris, pH 7.5, 150 mM NaCl, 5 mM MgCl₂, 0.5
227 mM EGTA, 1 mM EDTA, 0.5% SDS, 1% Triton X-100, and 1% sodium deoxycholate.
228 Complete protease inhibitor (Thermo Fisher Scientific), phosphatase inhibitor cocktail III
229 (Thermo Fisher Scientific), iodoacetamide (Sigma), and n-ethylmaleimide (Sigma) were
230 added to the homogenization buffer according to the manufacturer's instructions.
231 Tissues were disrupted using a mechanical homogenizer. Following homogenization,
232 samples were sonicated and centrifuged at 17000 x g for 10 min at 4°C to remove any
233 insoluble material, and supernatants were stored at -20°C. Protein concentrations were
234 determined using the BCA protein assay kit (Thermo Fisher Scientific).

235 **Immunoblotting**

236 Proteins were resolved on either 12% or 4-20% polyacrylamide gels and
237 transferred onto nitrocellulose membranes. A solution of 2% bovine serum albumin
238 (BSA) in tris-buffered saline with 0.1% Tween 20 (TBST) was used to block the
239 membranes. Primary and secondary antibodies (Abs) were diluted in a solution
240 containing 0.5% BSA in TBST. Primary Abs were used at a dilution of 1:1000 and
241 included: rabbit anti-HGS (Cell Signaling Technologies, RRID:AB_2798700), mouse
242 anti-HGS (Santa Cruz Technologies, sc-271925), mouse anti-MBP (Santa Cruz

243 Technologies, sc-271524), mouse anti-MPZ (Santa Cruz Technologies, sc-18531),
244 rabbit anti-ERBB2 (Cell Signaling Technologies, #4290), rabbit anti-pERBB2 (Cell
245 Signaling Technologies, #2243), rabbit anti-ERBB3 (Cell Signaling Technologies,
246 RRID:AB_10691324) , rabbit anti-pERBB3 (Cell Signaling Technologies,
247 RRID:AB_2099709), rabbit anti-AKT (Cell Signaling Technologies, RRID:AB_331152),
248 rabbit anti-pAKT308 (Cell Signaling Technologies, RRID:AB_330302), rabbit anti-
249 pAKT473 (Cell Signaling Technologies, #4060), rabbit anti-ERK (Cell Signaling
250 Technologies, #4695), rabbit anti-pERK (Cell Signaling Technologies, #4370), rabbit
251 anti-GSK3 β (Cell Signaling Technologies, #9315), rabbit anti-pGSK3 β (Cell Signaling
252 Technologies, #9323), rabbit anti-NF2 (Cell Signaling Technologies, #6995), rabbit anti-
253 pNF2 (Cell Signaling Technologies, #9163). Mouse anti-ACTB (Abcam,
254 RRID:AB_303668) was used as a loading control. The goat anti-mouse horseradish
255 peroxidase-conjugated secondary Ab (Southern Biotechnology Associates, #6420-05)
256 and goat anti-rabbit horseradish peroxidase-conjugated secondary Ab (Southern
257 Biotechnology Associates, #3030-05) were used at a 1:6000 dilution. SuperSignal West
258 Pico Chemiluminescent Substrate (Thermo Fisher Scientific) was applied to each
259 nitrocellulose membrane and allowed to incubate for 5 min before exposing to film. Blots
260 were cropped to show reactive bands.

261 **RNA-Seq library preparation and sequencing**

262 Total RNA from P14 sciatic nerves was isolated using RNA-STAT60 (Tel-Test).
263 mRNA sequencing was performed on the Illumina NextSeq500 as described by the
264 manufacturer (Illumina, Inc.). Briefly, RNA quality was assessed using the Agilent 2100
265 Bioanalyzer. RNA with a RNA Integrity Number (RIN) of ≥ 7.0 was used for sequencing

266 library preparation. RNA passing quality control was converted to a sequencing ready
267 library using the NEBNext Ultra II Directional RNA library kit as per the manufacturer's
268 instructions (New England Biolabs). The cDNA libraries were quantitated using qPCR in
269 a Roche LightCycler 480 with the Kapa Biosystems kit for Illumina library quantitation
270 prior to cluster generation. Cluster generation was performed according to the
271 manufacturer's recommendations for onboard clustering. We generated between 30 to
272 35 million paired-end 75 bp sequencing reads per sample for transcript level
273 abundance.

274 **Data assessment and systems biology analysis**

275 STAR (version 2.7.3a) was used to align the raw RNA-Seq fastq reads to the
276 GRCm38 p6 Release M24 reference genome from Gencode (Dobin et al., 2013).
277 Following alignment, HTSeq-count (version 0.13.5) was used to count the number of
278 reads mapping to each gene (Anders et al., 2015). Normalization and differential
279 expression was then applied to the count files using DESeq2 (Love et al., 2014). For
280 generating networks, a data set containing gene identifiers and corresponding
281 expression values was uploaded into Ingenuity Pathway Analysis. Each identifier was
282 mapped to its corresponding object in Ingenuity's Knowledge Base. A fold change cutoff
283 of ± 2 and $\text{padj} < 0.05$ was set to identify molecules whose expression was significantly
284 differentially regulated. These molecules, called Network Eligible molecules, were
285 overlaid onto a global molecular network developed from information contained in
286 Ingenuity's Knowledge Base. Networks of Network Eligible Molecules were then
287 algorithmically generated based on their connectivity. The Functional Analysis identified
288 the biological functions and/or diseases that were most significant to the entire data set.

289 Molecules from the dataset that met the fold change cutoff of ± 2 and $p_{adj} < 0.05$ and
290 that were associated with biological functions and/or diseases in Ingenuity's Knowledge
291 Base were considered for the analysis. Right-tailed Fisher's exact test was used to
292 calculate a p-value determining the probability that each biological function and/or
293 disease assigned to that data set was due to chance alone.

294 **Quantitative PCR**

295 Total RNA was isolated from the gastrocnemius muscles and sciatic nerves of
296 *Hgs^{fl}* and *P0CreHgs^{fl}* mice using RNA-STAT60 and reverse transcribed using the
297 Superscript VILO cDNA synthesis kit (Thermo Fisher Scientific). Individual gene assays
298 were purchased from Applied Biosystems and included *Achra* (Mm00431629_m1),
299 *Achrb* (Mm00680412_m1), *Achrg* (Mm00437419_m1), *Achre* (Mm00437411_m1),
300 *Nrg1* (Mm01212130_m1), *Cd44* (Mm01277165_m1), *Btc* (Mm00432137_m1),
301 *ErbB2* (Mm00658541_m1), *ErbB3* (Mm01159999_m1), *ErbB4* (Mm01256796_m1),
302 *Hdac1/2* (Mm02745760_g1), *Sox10* (Mm01300162_m1), *Nfatc4* (Mm00452375_m1),
303 *Sox2* (Mm03053810_s1), *Pou3f1* (Mm00456392_m1), *Pou3f2* (Mm00843777_s1), *c-*
304 *Jun* (Mm07296811_s1), *Krox20* (Mm00456650_m1), *Nab1* (Mm01257272_m1),
305 *Srebp* (Mm00550338_m1), *Mpz* (Mm00485141_g1), *Pmp22* (Mm01333393_m1)
306 and *Mbp* (Mm01266402_m1). The Taqman gene assay for *Actb* (Mm026195800_g1)
307 served as an internal control. qPCR results are shown as the average of 3 cDNA
308 amplifications generated from 3 mice performed in triplicate.

309 **Sciatic nerve immunohistochemistry.**

310 Sciatic nerves were rapidly dissected and submerged overnight in 4%
311 paraformaldehyde (Sigma) in PBS and cryoprotected in 30% sucrose (Fisher Scientific)

312 overnight before being embedded in optimal cutting temperature compound (Fisher
313 Scientific) and frozen at -80°C. Cryosections were cut at 10 µm on a Leica 1850
314 cryostat, mounted on Superfrost charged slides, and stored at -80°C. Nerve sections
315 were blocked with 10% normal goat serum, 1% BSA, and 0.1% Triton X-100. Primary
316 Abs and Alexa Fluor-labeled secondary Abs (Thermo Fisher Scientific, RRID:AB_
317 2534744 and RRID:AB_2536524) were diluted 1:500 in PBS containing 2% normal goat
318 serum, 0.1% BSA, and 0.1% Triton X-100. Primary mouse anti-HGS (Bean et al., 2000)
319 and rabbit anti-Ki67 (Abcam, RRID:AB_443209) Abs were incubated overnight at 4°C.
320 Sections were washed three times with PBS containing 0.1% Triton X-100 and then
321 incubated with secondary Abs for 1 h at room temperature. Sections were then washed
322 three times with PBS containing 0.1% Triton X-100 and stained with DAPI. Images were
323 acquired using a Zeiss LSM-800 Airyscan confocal microscope (Carl Zeiss).

324 Teased sciatic nerves were isolated from P14 mice and submerged in Bouin's
325 fixative (RICCA Chemical Company) for 15 min at 4°C. Nerves were then washed three
326 times in ice-cold PBS and stored overnight at 4°C. The perineurial sheath was then
327 removed, and axons were separated on Superfrost slides using a tuberculin needle.
328 Slides were dried overnight at room temperature and stored at -80°C. Nerves were then
329 permeabilized with methanol for 15 min at -20°C. Sections were blocked with 2.5%
330 normal donkey serum, 2.5% BSA, and 0.5% Triton X-100. Primary mouse anti-HGS
331 (Bean et al., 2000) and rabbit anti-EEA1 (Cell Signaling Technologies,
332 RRID:AB_11004515) Abs were diluted 1:200 in 2.5% normal donkey serum, 2.5% BSA,
333 and 0.5% Triton X-100 and incubated overnight at 4°C. Sections were washed three
334 times with PBS at room temperature and then incubated with secondary antibodies

335 labeled with Alexa Fluor dye (Thermo Fisher Scientific, RRID:AB_2534744 and
336 RRID:AB_2536524) for 1 h at room temperature. Sections were washed three times
337 with PBS and then stained with DAPI. Images were acquired using a Zeiss LSM-
338 800 Airyscan confocal microscope (Carl Zeiss).

339 **Muscle and neuromuscular junction (NMJ) analysis**

340 For whole-mount immunostaining, mice were euthanized and the tibialis anterior
341 muscles were rapidly dissected and fixed in 2% paraformaldehyde for 1 h at 4°C.
342 Muscles were teased into fiber bundles and then washed with wash buffer (PBS
343 containing 1% Triton X-100) three times at room temperature for 15 min. Muscle
344 bundles were then blocked with wash buffer containing 2% BSA and 4% normal goat
345 serum for 1 h. To label AChRs, samples were incubated with 1 µg/mL α-bungarotoxin
346 conjugated with tetramethylrhodamine isothiocyanate (Thermo Fisher Scientific) for 1 h.
347 After being washed three times at room temperature for 15 min with wash buffer,
348 muscle fibers were incubated with primary Abs for 2 days at 4°C.

349 Primary Abs were diluted 1:400 for mouse anti-neurofilament heavy chain and
350 1:200 for mouse anti-SV2 synaptic vesicle proteins (Developmental Studies Hybridoma
351 Bank) in PBS containing 1% BSA, 10% normal goat serum, and 0.1% Triton X-100.
352 After being washed three times for 15 min at room temperature, samples were
353 incubated with secondary Abs conjugated with Alexa Fluor 488 dye (Invitrogen) at a
354 1:500 dilution for 1 day at 4°C. Samples were then washed three times for 30 min at
355 room temperature, mounted in PBS containing 50% glycerol, and stored at -20°C.
356 Images were captured using a Zeiss LSM-800 Airyscan confocal microscope. The size
357 of all endplates within the area captured were determined by tracing the circumference

358 of the α -bungarotoxin-positive post-synaptic AChR cluster and computing the area using
359 ImageJ software. The extent of overlap between the pre- and post-synaptic structures
360 was determined by examining 100 randomly selected NMJs in each muscle (Seburn et
361 al., 2006). Junctions where the nerve completely overlapped the AChRs on the muscle
362 were defined as fully innervated, NMJs with vacant receptor territory were defined as
363 partially innervated, and AChR plaques with no nerve associated were defined as
364 denervated.

365 **Nerve electrophysiology**

366 Bilateral sciatic motor nerve conduction studies (Ubogu et al., 2012; Dong et al.,
367 2016; Dong et al., 2017) were performed on each mouse using a portable
368 Keypoint[®] v5.11 electrodiagnostic system (Alpine Biomed Corporation) with waveforms
369 displayed on a Tecra S3 LCD monitor (Toshiba America). The distal latency, distal and
370 proximal compound motor action potential (CMAP) amplitude and duration, conduction
371 velocity, and total waveform duration were recorded for each mouse. Recordings made
372 from both nerves were averaged for each animal.

373 **Data analysis**

374 Western blots were digitized, and band densities were quantified with UN-SCAN-
375 IT gel digitizing software (Silk Scientific). Pixel totals were recorded and normalized to
376 the level of ACTB. Protein levels were reported as pixel density relative to controls. An
377 unpaired Student's t-test was performed to determine statistical significance. All data
378 were analyzed using Prism Graphpad software by plotting the average +/- the standard
379 error of the mean. A minimum of 4 sciatic nerve extracts from each genotype were
380 analyzed for each protein of interest.

381 **Results**382 **Schwann cell-specific deletion of *Hgs***

383 Our previous studies demonstrated that a methionine to valine substitution in the
384 cargo-binding domain of HGS caused motor and sensory neuropathies in *teetering* mice
385 (Watson et al., 2015a). Because HGS function was altered in all cell types in the
386 *teetering* mice, we could not differentiate if the neurological defects were due to
387 disruption of HGS in neurons or in Schwann cells. We therefore created a mouse line
388 that specifically deleted *Hgs* in Schwann cells to test if the loss of HGS in Schwann cells
389 is sufficient to cause a peripheral neuropathy. To inactivate *Hgs* in Schwann cells, we
390 crossed *Hgs^{fl}* mice, in which exon 5 of *Hgs* is flanked by *loxP* sites, with *P0Cre*
391 transgenic mice that express Cre recombinase from the myelin protein zero promoter
392 (*Mpz/P₀*) (Feltri et al., 1999a). The *P0Cre* promoter has been extensively used to ablate
393 the expression of genes specifically within Schwann cells (Bolis et al., 2005; Berti et al.,
394 2011; Orita et al., 2013; Beirowski et al., 2014b; Grove et al., 2017; Alvarez-Prats et al.,
395 2018). In the resulting *P0CreHgs^{fl}* mice, Cre-mediated recombination deleted exon 5 of
396 the *Hgs* gene in Schwann cells, enabling us to investigate the role of HGS during
397 peripheral nerve myelination.

398 To assess Cre-mediated DNA recombination of the *Hgs^{fl}* allele, reverse
399 transcription PCR with primers that bordered exons 4 and 6 was used to examine RNA
400 from the sciatic nerves of P14 *P0CreHgs^{fl}* and *Hgs^{fl}* mice. Whereas a single band that
401 corresponds to the 634 bp DNA fragment expected from exons 4, 5 and 6 of *Hgs* was
402 produced from the *Hgs^{fl}* sciatic nerve RNA, two distinct DNA fragments were generated
403 from the RNA obtained from the sciatic nerves of the 2-week-old *P0CreHgs^{fl}* mice (Fig.

404 1A). The larger, less abundant band was the same size as that found in the *Hgs*^{fl}
405 controls, and the smaller, more prominent band was consistent with the expected 510
406 bp fragment that contains exons 4 and 6 but lacks exon 5 of *Hgs* (Fig. 1A). DNA
407 sequencing of the two fragments generated from the *P0CreHgs*^{fl} mice verified that the
408 larger band represented the typical splicing pattern of *Hgs*, while the faster migrating
409 band contained a deletion of exon 5 (Fig. 1B). Whereas the *Hgs*^{fl} allele is predicted to
410 generate a 776 amino acid protein, the deletion of exon 5 in the *P0CreHgs*^{fl} mice is
411 expected to result in a frame-shift mutation that truncates HGS after 140 amino acids.
412 Although we have not detected this truncated form in *P0CreHgs*^{fl} sciatic nerves using an
413 antibody that recognizes the N-terminus of HGS (Figure 1-1), this fragment of HGS
414 lacks the FYVE domain that is essential for HGS to bind to endosomes.

415 Immunoblot analysis confirmed reduced HGS expression in sciatic nerve extracts
416 from 1- to 4-week-old *P0CreHgs*^{fl} mice relative to controls (Fig. 1C and D). This
417 decrease in HGS expression was not observed in brain extracts from 4-week-old
418 *P0CreHgs*^{fl} mice (Fig. 1C and D), which is consistent with the specificity of the *P0Cre*
419 promoter for Schwann cells. Immunostaining for HGS also showed a substantial
420 reduction in HGS in teased sciatic nerves from 2-week-old *P0CreHgs*^{fl} mice compared
421 to controls. In control mice, HGS was detected in an expected punctate-like pattern in
422 the cytosol that partially overlapped the staining of the early endosomal antigen EEA1
423 (Fig. 1E).

424 A transcriptome database was recently generated to determine the
425 developmental and cellular profile of genes expressed in sciatic nerves (Gerber et al.,
426 2021). Examination of this database revealed that HGS is expressed in proliferating,

427 immature, promyelinating, mature, and non-myelinating Schwann cells (Fig. 1F). HGS
428 expression was also detected in perineurial cells, endoneurial cells, epineurial cells,
429 immune cells, pericytes, vascular smooth muscle cells and pericytes/endothelial cells
430 (Fig. 1F). Therefore, the low levels of HGS that we detected in the sciatic nerves of the
431 *P0CreHgs^{fl}* mice by both immunoblotting and immunofluorescence likely represent HGS
432 expression in these other cell types. This residual level of gene expression is similar to
433 what has been reported when *P0Cre* has been used to delete other floxed alleles
434 (Beirowski et al., 2014a; Gomez-Sanchez et al., 2015; Logan et al., 2017).

435 **Motor and sensory defects in *P0CreHgs^{fl}* mice**

436 *P0CreHgs^{fl}* mice were born at a Mendelian frequency and were indistinguishable
437 from control *Hgs^{fl}* mice at birth. Although no difference in body mass was detected at
438 one month of age, the *P0CreHgs^{fl}* mice were significantly smaller than controls by 4
439 months of age (Fig. 2A). In an open field assay to examine overall motor function, 4-
440 month-old *P0CreHgs^{fl}* mice traveled significantly less than controls (Fig. 2B and Figure
441 2-1), but no difference was observed in the average velocity of the *P0CreHgs^{fl}* mice
442 compared to controls (Fig. 2C). In addition, the grip strength of the *P0CreHgs^{fl}* mice
443 was significantly reduced at 4 months of age (Fig. 2D), and the mice demonstrated a
444 decreased ability to stay on a Rotarod at both 1 and 4 months of age compared to
445 controls (Fig. 2E). By 4 months of age, the *P0CreHgs^{fl}* mice also displayed decreased
446 tactile sensitivity when examined using the von Frey assay (Fig. 2F). These results
447 indicate that loss of HGS in Schwann cells results in both motor and sensory deficits in
448 the *P0CreHgs^{fl}* mice.

449

450 **Motor nerve electrophysiology**

451 To determine whether Schwann cell-specific loss of HGS altered the
452 electrophysiological properties of the peripheral nerves, we measured the amplitudes
453 and durations of the compound muscle action potentials (CMAPs) of the calf muscles,
454 the distal latency, and the deduced velocities following distal and proximal sciatic nerve
455 stimulation (Fig. 3). Both distal and proximal CMAP amplitudes, which indirectly
456 measure the number of functional myelinated motor axons, were markedly reduced in 4-
457 month-old *P0CreHgs^{fl}* mice compared to controls (Fig. 3A and B). In addition, the distal
458 and proximal CMAP durations were also significantly increased in the *P0CreHgs^{fl}* mice
459 (Fig. 3C and D), indicating conduction slowing and/or conduction block of myelinated
460 motor axons. Consistent with these findings, the distal CMAP latency was significantly
461 prolonged (Fig. 3E), and the conduction velocity was significantly reduced (Fig. 3F) in
462 the *P0CreHgs^{fl}* mice compared to controls, both of which measure the conduction of the
463 fastest conducting motor axons. Together, these abnormal electrophysiological
464 properties indicate that Schwann cell loss of HGS causes a demyelinating peripheral
465 neuropathy.

466 **Delayed myelination in HGS-deficient Schwann cells**

467 We used transmission electron microscopy to examine transverse sections of
468 sciatic nerves from *P0CreHgs^{fl}* and *Hgs^{fl}* mice at P7, P14, P28 and P120 (Fig. 4A-C). In
469 *Hgs^{fl}* control mice, over 75% of the large diameter axons (>1 micron) were myelinated at
470 P7, and the proportion of myelinated axons progressively increased so that almost all of
471 the large caliber axons were myelinated by P28 (Fig. 4A and B), which is consistent with
472 what has been reported for wild type mice (Hahn et al., 1987). In contrast, the number

473 of myelinated axons in the sciatic nerves of *P0CreHgs^{fl}* mice was significantly reduced
474 at all ages examined (Fig. 4A and B). Instead of the typical myelinated axons, many
475 promyelinated axons were observed in the sciatic nerves from the P7, P14 and P28
476 *P0CreHgs^{fl}* mice; these are axons that are ensheathed in a 1:1 ratio by Schwann cells
477 but are not myelinated (Arroyo et al., 1998). Although promyelinated axons could also
478 be observed in *P0CreHgs^{fl}* mice at P120, due to the presence of basal lamina onion
479 bulbs around some of these axons (Fig. 4A), they may also be in the process of being
480 re-ensheathed following segmental demyelination. The myelin sheaths from *P0CreHgs^{fl}*
481 sciatic nerves were also significantly thinner than controls at all ages examined (Fig.
482 4C). The reduced number of myelinated axons and the thinner myelin sheaths in
483 *P0CreHgs^{fl}* nerves correlated with reduced levels of myelin basic protein (MBP) and
484 myelin protein zero (MPZ) in the sciatic nerves of *P0CreHgs^{fl}* mice (Fig. 4D).

485 Since a change in axon diameter has been reported in a number of peripheral
486 neuropathies, we compared the frequency distribution of axonal diameters found in the
487 sciatic nerves of *P0CreHgs^{fl}* mice with controls. We found a significant reduction in
488 axonal diameter at P7, P14 and P28 (Fig. 4E), which could also contribute to the
489 hypomyelination observed in the *P0CreHgs^{fl}* mice. To determine if defective myelination
490 in the *P0CreHgs^{fl}* mice also results in axonal loss, we measured the numbers of large
491 caliber axons in sciatic nerve sections from control and *P0CreHgs^{fl}* mice at 4 months of
492 age. Despite a significant reduction in myelination (Fig. 4B), the number of axons
493 greater than 1 micron in diameter was not significantly different in the *P0CreHgs^{fl}* sciatic
494 nerves compared to controls (Fig. 4F). There was also no significant difference in radial

495 sorting of large diameter axons or the number of unmyelinated axon bundles in the
496 sciatic nerves of P3 *P0CreHgs^{fl}* mice compared to controls (Fig. 4G-I).

497 In addition to causing delayed and reduced myelination, loss of HGS in Schwann
498 cells resulted in aberrantly folded myelin sheaths. These were evident in the sciatic
499 nerves of both P28 and 6-month-old *P0CreHgs^{fl}* mice (Fig. 5A-C). Conspicuously folded
500 myelin sheaths have been reported in humans and animal models of other inherited
501 demyelinating neuropathies (Azzedine et al., 2003b; Bolino et al., 2004; Bolis et al.,
502 2005; Robinson et al., 2008; Pereira et al., 2012) and are thought to be due to Schwann
503 cell autonomous deficits. Thus, HGS is required for both the proper induction of
504 myelination and the formation of structurally normal myelin sheaths.

505 **Loss of HGS in Schwann cells alters NMJ and muscle development**

506 Several reports have indicated developmental impairment and reduced synaptic
507 transmission at the NMJ in mouse models of CMT (Yin et al., 2004; Ang et al., 2010;
508 Sleigh et al., 2014; Spaulding et al., 2016; Cipriani et al., 2018; Nandini et al., 2019). To
509 investigate if loss of HGS in Schwann cells also disrupts the NMJ, we first examined the
510 gastrocnemius muscles and found a significant decrease in muscle mass in 4-month-old
511 *P0CreHgs^{fl}* mice compared to controls (Fig. 6A). As impaired innervation can result in
512 reduced muscle development and upregulated expression of AChRs (Evans et al.,
513 1987; Goldman et al., 1988; Witzemann, 1989; Ang et al., 2010), we next measured the
514 *AChR* α , β , ϵ and γ subunit mRNA levels in the gastrocnemius muscles of 4-month-old
515 *Hgs^{fl}* and *P0CreHgs^{fl}* mice. Although no differences were observed in *AChR* α or ϵ
516 mRNA levels, there was a significant increase in the levels of both *AChR* β and
517 γ subunit mRNAs in *P0CreHgs^{fl}* mice relative to controls (Fig. 6B). Since skeletal muscle

518 denervation in animal models results in muscle atrophy and a significant increase in the
519 expression of the *AChR* γ subunit (Witzemann, 1989; Eiber et al., 2019; Cetin et al.,
520 2020), our data suggests that Schwann cell loss of HGS impacts synaptic transmission
521 at the NMJ (Goldman et al., 1988; Adams et al., 1995; Kong et al., 2009; Vaden et al.,
522 2015; Watson et al., 2015a).

523 To examine motor endplate structure in the *Hgs^{fl}* and *P0CreHgs^{fl}* mice, we
524 identified motor axons by immunostaining the tibialis anterior muscles for neurofilament
525 (NF) and synaptic vesicle protein 2 (SV2) and labeled the AChRs with FITC-conjugated
526 α -bungarotoxin (Fig. 6C). At 4 months of age, there was a reduction in fully innervated
527 NMJs and a corresponding increase in partially innervated NMJs in *P0CreHgs^{fl}* mice
528 compared to controls (Fig. 6C and D). These results suggest that the impaired *AChR*
529 expression and reduced muscle mass in the *P0CreHgs^{fl}* mice are due to changes in
530 NMJ integrity.

531 **Transcriptome analysis of HGS-deficient sciatic nerves**

532 To investigate the cause of arrested sciatic nerve myelination in the *P0CreHgs^{fl}*
533 mice, we performed transcriptome analysis on sciatic nerve RNA from P14 *P0CreHgs^{fl}*
534 and *Hgs^{fl}* control mice. Principal component analysis demonstrated that the results from
535 both the control and the *P0CreHgs^{fl}* sciatic nerves clustered into two distinct groups for
536 each genotype (Fig. 7A). Bioinformatics analysis revealed that the expression of 2469
537 genes was altered at least 2-fold in the *P0CreHgs^{fl}* sciatic nerves compared to controls
538 (Fig. 7B and Figure 7-1), and the top 50 upregulated and top 50 downregulated genes
539 are shown in figures 7C and D. Gene Ontology and pathway analysis revealed an

540 enrichment in genes that regulate cell proliferation, gliogenesis and myelination in the
541 sciatic nerves of the *P0CreHgs^{fl}* mice (Fig. 7E and Figure 7-2, 7-3 and 7-4).

542 **Increased cell-proliferation in HGS-deficient sciatic nerves**

543 Transcriptome analysis of sciatic nerves from *P0CreHgs^{fl}* mice demonstrated a
544 striking enrichment of genes involved in cell proliferation and cell cycle control. To
545 investigate if the arrested myelination observed in the *P0CreHgs^{fl}* mice was due to
546 changes in cell proliferation and/or Schwann cell differentiation, we first compared Ki67
547 staining in control and *P0CreHgs^{fl}* sciatic nerves at P7 and P14. Consistent with a
548 previous report (Brown and Asbury, 1981), we observed the expected reduction in
549 proliferating cells in sciatic nerves from control mice at P14 compared to P7. Although
550 the percentage of Ki67 positive cells was not statistically different between the
551 *P0CreHgs^{fl}* mice and controls at P7 (Fig. 8A and B), there was a significant increase in
552 the number of proliferating cells in the sciatic nerves of the *P0CreHgs^{fl}* mice compared
553 to controls at P14 (Fig. 8A and C). These cells likely represent either proliferating
554 Schwann cells or infiltrating immune cells. A similar increase in the number of Ki67
555 positive cells has previously been found in other animal models of demyelinating
556 neuropathies (Perkins et al., 1981; Sancho et al., 2001) and is consistent with delayed
557 Schwann cell maturation.

558 Schwann cell differentiation is accompanied by a well-described and distinct
559 pattern of gene expression that defines immature Schwann cells, promyelinating
560 Schwann cells and myelinating Schwann cells (Jessen and Mirsky, 2005; Salzer, 2015).
561 To confirm our RNA transcriptome analysis that suggests a block in Schwann cell
562 maturation in the *P0CreHgs^{fl}* mice, we examined the expression of several markers of

563 immature, promyelinating and myelinating Schwann cells from RNA isolated from the
564 sciatic nerves of P14 *P0CreHgs^{fl}* and *Hgs^{fl}* mice using qPCR. Although we did not
565 observe any differences in the expression of the immature Schwann cell markers
566 *Hdac1*, *Sox10* or *Nfatc4* (Fig. 8D), there was an increase in the levels of several
567 promyelinating mRNAs, including *Sox2*, *Pou3f1*, *Pou3f2*, and *c-Jun* in the sciatic nerves
568 of the *P0CreHgs^{fl}* mice as compared to controls (Fig. 8E). In addition, the mRNA levels
569 for *Egr2*, *Nab1*, *Srebp1*, *Mpz*, *Pmp22*, and *Mbp*, which are markers of myelinating
570 Schwann cells, were reduced in the sciatic nerves of P14 *P0CreHgs^{fl}* mice as compared
571 to controls (Fig. 8F). Consistent with our findings on the level of HGS at P14, the level of
572 *Hgs* mRNA was reduced by 70% in the *P0CreHgs^{fl}* sciatic nerves (Fig. 8F). Thus, the
573 altered gene expression in HGS-deficient Schwann cells corresponds with the increase
574 in promyelinating Schwann cells observed in the sciatic nerves of the P14 *P0CreHgs^{fl}*
575 mice (Fig. 4A).

576 **Alterations in the ERBB2/3 pathway in HGS-deficient Schwann cells**

577 Our transcriptome analysis showed that the NRG1/ERBB signaling pathway was
578 significantly upregulated in the sciatic nerves of the *P0CreHgs^{fl}* mice (Figure 7-1 and 7-
579 2). Further examination of the mRNA levels of components in this pathway validated
580 the RNA-Seq results and demonstrated that the levels of *ErbB3*, *Btc*, *Nrg1*, and *Cd44*
581 were all significantly increased, while the level of *ErbB2* was unchanged and the level of
582 *ErbB4* was reduced, in the sciatic nerves of P14 *P0CreHgs^{fl}* mice compared to controls
583 (Fig. 9A), indicating that Schwann cell loss of HGS disrupts the regulation of
584 components of the ERBB signaling pathway.

585 Since the ERBB2/3 receptors play an essential role in Schwann cell development
586 and myelination (Riethmacher et al., 1997; Garratt et al., 2000; Brinkmann et al., 2008),
587 we examined whether loss of HGS altered either the levels or activation of proteins in
588 the ERBB pathway. The activation of the ERBB2/3 receptors by NRG1 results in their
589 autophosphorylation, which can be measured using phospho-specific ERBB2/3 Abs.
590 Although there was no difference in the total levels of ERBB2 within the first 2 weeks of
591 postnatal development (Fig. 9B and C), the levels of phosphorylated ERBB2 were
592 significantly elevated in *P0CreHgs^{fl}* mice compared to controls at both P7 and P14 (Fig.
593 9B and D). In contrast, we observed a significant increase in the levels of total ERBB3
594 in the sciatic nerve extracts of the *P0CreHgs^{fl}* mice at P14, but not at P7, when
595 compared to controls (Fig. 9E and F). Although we observed an increase in the levels of
596 pERBB3 in the sciatic nerves of the P14 *P0CreHgs^{fl}* mice, this difference was not
597 significant when normalized against the total ERBB3 levels detected in the mice (Fig.
598 9G). These results are consistent with the transcriptome and qPCR results of increased
599 levels of *Erb3* mRNA without a corresponding change in *Erb2* mRNA in the sciatic
600 nerves of P14 *P0CreHgs^{fl}* mice. Taken together, these data suggest that loss of HGS
601 altered the expression of components of the ERBB pathway and the activation of the
602 ERBB2 receptor in Schwann cells.

603 **Loss of HGS impairs AKT signaling**

604 The ERBB2/3 receptors activate several intracellular signaling pathways,
605 including the PI3K-AKT kinase and ERK pathways, which are essential for Schwann cell
606 development and myelination (Monje et al., 2006; Monje et al., 2008; Syed et al., 2010;
607 Newbern et al., 2011; Heller et al., 2014; Domenech-Estevéz et al., 2016). To determine

608 whether loss of HGS in Schwann cells affects these pathways, we examined the
609 activated state of these kinases using Abs that recognize the phosphorylated forms of
610 AKT and ERK. As AKT is phosphorylated at T308 by PDK1 and at S473 by mTORC2,
611 these experiments examined the phosphorylated state of AKT at both of these
612 positions. We found that pAKT (T308) was significantly reduced in sciatic nerve extracts
613 from P14 *P0CreHgs^{fl}* mice compared to controls (Fig. 9H and I). In contrast, no
614 significant differences were observed in pAKT (S473), pERK, or pGSK3 β expression in
615 the sciatic nerves from P14 *P0CreHgs^{fl}* mice and controls (Fig. 9H and I). Although
616 HGS has also been shown to interact with NF2 and regulate its signaling (Gutmann et
617 al., 2001; Sun et al., 2002), when we examined the effect of Schwann cell-specific loss
618 of HGS on NF2, there was no significant difference in the levels of either total or
619 activated NF2 proteins in the sciatic nerves of the P14 *P0CreHgs^{fl}* mice compared to
620 controls (Fig. 9H and I).

621

622 Discussion

623 The identification of endosomal genes linked to demyelinating forms of CMT
624 motivated our interest to understand the role of the endocytic pathway during
625 myelination. In this study, we used a targeted Schwann cell-specific deletion of HGS to
626 disrupt the endosomal sorting pathway in Schwann cells and examine its effect on
627 peripheral nerve myelination. We found that loss of HGS delayed the transition of
628 promyelinating Schwann cells to myelinating Schwann cells and resulted in
629 hypomyelination and aberrant myelination of sciatic nerves, demonstrating that
630 endosomal sorting is required for the normal development of myelinating Schwann cells.

631 Loss of HGS also resulted in increased levels of phosphorylated ERBB2 receptors,
632 increased levels of total ERBB3, and a reduction in the steady-state levels of
633 pAKT(T308), which reinforces the idea that the ESCRT pathway regulates the sorting of
634 the ERBB2/3 receptors and supports a growing body of evidence that ERBB2/3
635 signaling is disrupted in some demyelinating forms of CMT (Lee et al., 2017).

636 HGS is expressed in multiple cell types within the nervous system, including
637 neurons and Schwann cells. In our previous report (Watson et al., 2015b), we showed
638 that a point mutation in the cargo-binding domain of HGS resulted in thicker myelin
639 sheaths in the sciatic nerves of *teetering* mice. This phenotype differs from the
640 hypomyelination defects that occur when HGS is deleted specifically within Schwann
641 cells. However, as the *teetering* mutation also has dominant effects on both tactile
642 sensitivity and exercise-induced ataxia (Meier, 1967; Watson et al., 2015a), it is likely
643 that the differences in myelination between the two mouse models are due to a loss of
644 function of HGS in the *P0CreHgs^{f/f}* mice, as opposed to a gain of function in the
645 *teetering* mice, as well as the fact that the *teetering* mutation is expressed in both
646 neurons and Schwann cells.

647 The development of myelinating Schwann cells requires both extrinsic and
648 intrinsic cellular signals (Jessen and Mirsky, 2008). These signals control the
649 expression of both positive and negative regulators of myelination and ultimately
650 determine the onset and extent of myelination. In the *P0CreHgs^{f/f}* mice, loss of HGS
651 disrupted the maturation of myelinating Schwann cells, presumably by preventing the
652 repression of multiple negative regulators of myelination, such as *Sox-2*, *c-Jun* and
653 *Pax3*, and/or preventing the induction of *Egr2*, a transcriptional factor required for

654 myelination (Topilko et al., 1994; Decker et al., 2006). Similar to what we observed in
655 the HGS-deficient Schwann cells, overexpression of Sox-2 in Schwann cells inhibited
656 the induction of myelin proteins, increased cell proliferation and caused severe
657 hypomyelination (Roberts et al., 2017). These findings suggest that endosomal sorting
658 regulates essential cell signaling events that are required for the induction of
659 myelination.

660 Neuregulin 1 signaling through the ERBB2/3 receptors is critical for many
661 aspects of Schwann cell development, including cell proliferation, migration along
662 peripheral axons and the induction of myelination (Newbern and Birchmeier, 2010;
663 Salzer, 2015). As deficits in the ERBB2/3 signaling pathway are thought to contribute to
664 peripheral neuropathies, these receptors are seen as potential therapeutic targets for
665 the treatment of CMT (Massa et al., 2006; Fledrich et al., 2014; Lee et al., 2016, 2017).
666 A recent report demonstrated that HGS interacts with ERBB3 (Fosdahl et al., 2017),
667 suggesting that the ERBB3 receptor is a substrate for the ESCRT pathway in Schwann
668 cells. Our finding that loss of HGS increased ERBB3 levels without altering the steady-
669 state level of ERBB2 adds further support to the idea that HGS specifically traffics the
670 ERBB3 receptor through the endolysosomal pathway. Since the ERBB2/3 receptors are
671 thought to be internalized and trafficked as a heterodimer to the endosome (Sorkin and
672 Goh, 2009; Bertelsen and Stang, 2014), our data support the idea that these receptors
673 may dissociate and be sorted independently on the endosome (Lenferink et al., 1998).
674 While greater levels of phosphorylated ERBB2 is indicative of increased activation of
675 these receptors and is associated with enhanced ERBB signaling, we did not observe
676 any increases in phosphorylated AKT or ERK that would suggest activation of these

677 downstream signaling pathways in the sciatic nerves of the *P0CreHgs^{fl}* mice. Instead,
678 we detected decreased levels of pAKT(T308) in HGS-deficient sciatic nerves. A
679 decrease in pAKT(T308) levels was also observed in the sciatic nerves of mice with a
680 deletion of Tuberous Sclerosis Complex Subunit 1 in Schwann cells that caused
681 hyperactivation of the mTOR pathway during development (Figlia et al., 2017),
682 suggesting the presence of an inhibitory feed-back loop that regulates the PI3K
683 pathway. It is possible that the increased activation of pERBB2 in the *P0CreHgs^{fl}* mice
684 may therefore have activated an inhibitory feedback loop leading to a reduction in
685 pAKT(308) (Figlia et al., 2018). Alternatively, AKT can be activated on the endosome
686 (Palfy et al., 2012; Ebner et al., 2017; Sugiyama et al., 2019), it is possible that impaired
687 trafficking of the ERBB2/3 receptors in *P0CreHgs^{fl}* mice disrupted this signaling
688 pathway in Schwann cells. In a similar manner, HGS is required for the activation of
689 signaling pathways downstream of the bone morphogenic receptor by acting as a
690 scaffold to recruit TAK1 and SMAD1/5/8 signaling complexes to the endosome (Miura
691 and Mishina, 2011a).

692 We observed an increased number of myelin outfoldings in the sciatic nerves of
693 HGS-deficient mice at both P28 and 6-months of age, and this finding suggests that
694 HGS is required for the proper formation and maintenance of myelin sheaths. Myelin
695 outfoldings are characteristic of CMT4B1 and CMT4B2, both of which are severe
696 demyelinating neuropathies (Azzedine et al., 2003a; Bolino et al., 2004; Bolis et al.,
697 2005; Delague et al., 2007; Robinson et al., 2008; Horn et al., 2012a) caused by
698 mutations in the Myotubularin-related protein 2 (MTMR2) and 13 (MTMR13),
699 respectively. MTMRs catalyze the dephosphorylation of phospholipids (Bolis et al.,

700 2007), which are docking sites for the recruitment of signaling molecules to internal
701 membranes. HGS possesses a FYVE domain, which binds PI(3)P and is necessary for
702 its association with the endosome (Komada and Soriano, 1999). It is interesting to note
703 that, like our HGS-deficient Schwann cells, loss of MTMR2 leads to myelin outfoldings
704 and increased levels of pERBB2 (Bolino et al., 2004; Bolino et al., 2016).
705 Downregulation of NRG1 signaling in *Mtmr2* knockout Schwann cells rescues the
706 myelin outfoldings, suggesting that deficits in phospholipid signaling can result in
707 localized changes in ERBB signaling and focal enhancement in myelination (Bolino et
708 al., 2016). We speculate that, in a similar manner, loss of HGS disrupts the sorting of
709 ERBB receptors, leading to enhanced focal myelination and the production of myelin
710 outfoldings. Future studies will examine if these outfoldings are localized to the
711 paranodal regions of *P0CreHgs^{fl}* mice, as is observed in the MTMR2-deficient mice.

712 As a master regulator of endosomal sorting (Kobayashi et al., 2005; Komada and
713 Kitamura, 2005), the requirements of HGS during peripheral nerve myelination are likely
714 to extend beyond those of just the ERBB2/3 receptors. However, the studies detailed in
715 this report provide evidence for the requirement of endosomal sorting of the ERBB2/3
716 receptors during peripheral nerve myelination and offer possible new targets for
717 therapeutic intervention in the treatment of peripheral neuropathies.

718

719 **Figure Legends**

720 Figure 1. Schwann cell-specific deletion of *Hgs*. (A). Agarose gel electrophoresis of the
721 RT-PCR products generated from the sciatic nerves of postnatal day (P) 14 *Hgs^{fl}* and
722 *P0CreHgs^{fl}* mice using primers that flank exons 4 and 6. The wild type *Hgs^{fl}* allele
723 contains exons 4, 5, and 6 of *Hgs* whereas the conditional allele generated from Cre-
724 mediated deletion of exon 5 only contains exons 4 and 6 as confirmed by (B) DNA
725 sequence analysis of the RT-PCR products showing the splicing pattern of the *Hgs*
726 mRNA. The arrows indicate the splice site junctions between either exons 4 and 5 in the
727 wild type allele or exons 4 and 6 in the conditional allele. (C) Representative
728 immunoblot and (D) quantitation showing reduced HGS levels in sciatic nerve extracts
729 from *P0CreHgs^{fl}* (*P0Cre+*) mice at P7 ($p = 4.61 \times 10^{-6}$), P14 ($p = 1.19 \times 10^{-6}$), and P28
730 ($p = 8.58 \times 10^{-6}$) but not in total brain extracts from P28 *P0CreHgs^{fl}* mice ($p = 0.26$)
731 relative to *Hgs^{fl}* controls (*P0Cre-*). ACTB was used as a loading control. Data are shown
732 as mean \pm SEM, $n = 3$.

733 Student's t-test was used to determine whether there was a significant difference in the
734 means of the datasets. (E) Immunofluorescence showing localization of HGS (green),
735 EEA1 (red) and DNA (DAPI, blue) in teased sciatic nerve sections from P14 *P0CreHgs^{fl}*
736 and *Hgs^{fl}* control mice. (F) Transcriptomics of sciatic nerves demonstrating HGS
737 expression in proliferating Schwann cells (prol. SC), immature Schwann cells (iSC),
738 promyelinating Schwann cells (pmSC), mature Schwann cells (mSC), transition
739 Schwann cells (tSC), non-myelinating (Remak) Schwann cells (nm(R)SC), perineurial
740 cells (PnC), endoneurial cells (EnC), epineurial cells (EpC), immune cells (IC), pericytes
741 and vascular smooth muscle cells (Per/VSMC) and pericytes/endothelial cells (Per/EC*)

742 over various stages of postnatal development (Gerber et al., 2021). Representative
743 immunoblot using an antibody recognizing the amino-terminus of HGS is shown in
744 Extended data Figure 1-1.

745 Figure 2. Motor and sensory function in *Hgs^{fl}* and *P0CreHgs^{fl}* mice. (A) Total body mass
746 (1 month $p = 0.62$, 4 month $p = 0.035$), (B) distance traveled in open field (1 month $p =$
747 0.53 , 4 month $p = 0.0087$), (C) average velocity in open field (1 month $p = 0.32$, 4 month
748 $p = 0.42$), (D) fore-limb grip strength (grams force(gf)) (1 month $p = 0.16$, 4 month $p =$
749 8.66×10^{-5}), and (E) latency to fall during rotarod analysis (1 month $p = 0.0043$, 4 month
750 $p = 1.0 \times 10^{-5}$) of *Hgs^{fl}* and *P0CreHgs^{fl}* mice. (F) Mechanical allodynia determined by
751 von Frey assay of *Hgs^{fl}* and *P0CreHgs^{fl}* mice ($p = 1.4 \times 10^{-4}$). Data are shown as mean
752 \pm SEM, $n \geq 5$ mice per genotype. Mann-Whitney test was used to determine whether
753 there was a significant difference in the means of the datasets. Representative open
754 field traces for 4 month-old *Hgs^{fl}* and *P0CreHgs^{fl}* mice are shown in Extended data
755 Figure 2-1.

756

757 Figure 3. Sciatic nerve electrophysiology in 4-month-old *Hgs^{fl}* and *P0CreHgs^{fl}* mice. (A)
758 Amplitude of distal CMAP ($p = 1.08 \times 10^{-5}$), (B) amplitude of proximal CMAP ($p = 1.1 \times$
759 10^{-5}), (C) distal total waveform duration ($p = 2.02 \times 10^{-11}$), (D) proximal total waveform
760 duration ($p = 1.08 \times 10^{-5}$), (E) distal latency ($p = 0.021$), and (F) conduction velocity ($p =$
761 1.1×10^{-5}) measured from both the right and left sciatic nerves and averaged for each
762 *Hgs^{fl}* and *P0CreHgs^{fl}* mouse. Data are shown as mean \pm SEM, $n = 10$ mice per
763 genotype.

764 Mann-Whitney test was used to determine whether there was a significant difference in
765 the means of the datasets.

766

767 Figure 4. Hypomyelination of sciatic nerves in *P0CreHgs^{fl}* mice. (A) Representative
768 electron micrographs of sciatic nerves from P7, P14, P28 and P120 *Hgs^{fl}* and
769 *P0CreHgs^{fl}* mice. Arrows indicate basal lamina onion bulbs. (B) Quantitation of the
770 percent of myelinated axons (P7 $p = 2.11 \times 10^{-5}$, P14 $p = 1.48 \times 10^{-4}$, P28 $p = 3.92 \times$
771 10^{-5} , P120 $p = 1.48 \times 10^{-4}$) and (C) the g-ratio (P7 $p = 3.0 \times 10^{-6}$, P14 $p = 3.23 \times 10^{-8}$,
772 P28 $p = 4.4 \times 10^{-5}$, P120 $p = 0.0021$) in sciatic nerves from *Hgs^{fl}* and *P0CreHgs^{fl}* mice.
773 Data are shown as mean \pm SEM, $n = 4$. Student's t-test was used to determine whether
774 there was a significant difference in the means of the datasets. (D) Representative
775 immunoblots showing the levels of myelin basic protein (MBP) and myelin protein zero
776 (MPZ) from sciatic nerve extracts of P7, P14, P28, and P120 *Hgs^{fl}* and *P0CreHgs^{fl}* mice.
777 ACTB was used as a loading control. (E) Cumulative frequency plots showing the
778 distribution of axon size in *Hgs^{fl}* and *P0CreHgs^{fl}* mice at P7 ($p = 4.61 \times 10^{-6}$), P14 ($p =$
779 1.19×10^{-6}), and P28 ($p = 8.85 \times 10^{-5}$). The Kolmogorov-Smirnov test was used to
780 determine significance. $n = 4$. (F) Quantitation of axons > 1 micron in sciatic nerves
781 from 4-month-old *Hgs^{fl}* and *P0CreHgs^{fl}* mice ($p = 0.22$). Data are shown as mean \pm
782 SEM, $n = 3$. Student's t-test was used to determine whether there was a significant
783 difference in the means of the datasets. (G) Representative electron micrograph of axon
784 bundles and quantitation of (H) axons per bundle ($p = 0.9287$, $n = 3$) and (I) axon
785 bundles per $100 \mu\text{m}^2$ ($p = 0.93$, $n = 4$) from sciatic nerves of P3 *Hgs^{fl}* and *P0CreHgs^{fl}*

786 mice. Data are shown as mean \pm SEM. Student's t-test was used to determine whether
787 there was a significant difference in the means of the datasets.

788

789 Figure 5. Deletion of HGS in Schwann cells leads to aberrant myelination. (A)
790 Representative electron micrographs of sciatic nerve sections from P28 and P180 *Hgs^{fl}*
791 and *P0CreHgs^{fl}* mice. Quantitation of myelin outfoldings in (B) P28 ($p = 0.0002$) and (C)
792 P180 ($p = 0.0023$) mice. Data are plotted as the percentage of fibers that were found to
793 be defective and are shown as mean \pm SEM, $n = 4$. Student's t-test was used to
794 determine whether there was a significant difference in the means of the datasets.

795

796 Figure 6. Effects of HGS deletion in Schwann cells on gastrocnemius mass, motor
797 endplate structure and *AChR* expression. (A) Gastrocnemius muscle mass from 4-
798 month-old *Hgs^{fl}* and *P0CreHgs^{fl}* mice ($p = 0.0020$). Data are plotted as mean \pm SEM, n
799 = 6 mice per genotype. Student's t-test was used to determine whether there was a
800 significant difference in the means of the datasets. (B) qPCR analysis of *AChR- α* ($p =$
801 0.068), *AChR- β* ($p = 3.0 \times 10^{-5}$), *AChR- ϵ* ($p = 0.57$), and *AChR- γ* ($p = 5.0 \times 10^{-5}$)
802 mRNAs from the gastrocnemius muscles of 4-month-old *Hgs^{fl}* and *P0CreHgs^{fl}* mice.
803 Data are plotted relative to the amount detected in *Hgs^{fl}* controls and are shown as
804 mean \pm SEM, $n = 3$. Student's t-test was used to determine whether there was a
805 significant difference in the means of the datasets. (C) Tibialis anterior muscles from 4-
806 month-old *Hgs^{fl}* and *P0CreHgs^{fl}* mice stained with Abs for neurofilament (NF) and the
807 synaptic vesicle protein 2 (SV2) to detect motor neuron terminals (green) and with
808 TRITC-labeled α -bungarotoxin to detect AChRs (red). (D) Quantification of NMJs

809 revealed that 89.97% of the NMJs were fully innervated and 10.03% of the NMJs were
810 partially innervated in the *Hgs^{fl}* mice, while 77.45% of the NMJs were fully innervated (p
811 = 0.0036) and 22.55% were partially innervated ($p = 0.0046$) in the *P0CreHgs^{fl}* mice at 4
812 months of age. Data are plotted as mean \pm SEM, $n = 4$ mice per genotype. Student's t -
813 test was used to determine whether there was a significant difference in the means of
814 the datasets.

815

816 Figure 7. Transcriptome analysis of *Hgs^{fl}* and *P0CreHgs^{fl}* sciatic nerves. (A) Principal
817 component analysis results show that gene expression in P14 *Hgs^{fl}* and *P0CreHgs^{fl}*
818 sciatic nerves segregate into two separate groups for each genotype. (B) Volcano plot
819 of transcriptome data displaying the pattern of genes altered at least 2-fold in sciatic
820 nerves of P14 *P0CreHgs^{fl}* mice compared to *Hgs^{fl}* controls ($p \leq 0.05$). Heat map of the
821 top 50 significantly (C) upregulated and (D) downregulated genes in the sciatic nerves
822 of P14 *P0CreHgs^{fl}* mice compared to *Hgs^{fl}* controls. Gene Ontology showing the (E)
823 biological processes altered in the *P0CreHgs^{fl}* sciatic nerves compared to controls. $n =$
824 2 mice per genotype. DESeq2 annotated results with normalized counts for P14 *Hgs^{fl}*
825 and *P0CreHgs^{fl}* transcriptome analysis are shown in Extended data Figure 7-1. Gene
826 Ontology analysis describing Biological Pathways, Cellular Components and Molecular
827 Functions altered in the *P0CreHgs^{fl}* sciatic nerves are shown in Extended data Figure 7-
828 2, 7-3 and 7-4 respectively.

829

830 Figure 8. Maturation deficits in HGS-deficient Schwann cells. (A) Sciatic nerve
831 sections from P7 and P14 *Hgs^{fl}* and *P0CreHgs^{fl}* mice were stained for the proliferating

832 antigen marker Ki67 (red) and with DAPI to detect DNA (blue). Quantitation of the
833 number of proliferating (Ki67-positive) nuclei from (B) P7 ($p = 0.12$) and (C) P14 ($p =$
834 4.51×10^{-8}) *Hgs^{fl}* and *P0CreHgs^{fl}* mice. Data are shown as mean \pm SEM, $n = 4$ mice per
835 genotype. Student's t-test was used to determine whether there was a significant
836 difference in the means of the datasets. Quantitation of mRNA levels in the sciatic
837 nerves of P14 *P0CreHgs^{fl}* mice for genes that serve as markers of (D) immature (*Hdac1*
838 $p = 0.77$, *Sox10* $p = 0.15$, *Nfatc4* $p = 0.50$), (E) promyelinating (*Sox2* $p = 1.0 \times 10^{-4}$,
839 *Pou3f1* $p = 1.0 \times 10^{-4}$, *Pou3f2* $p = 8.0 \times 10^{-4}$, *c-Jun* $p = 0.0032$), and (F) myelinating
840 (*Egr2* $p = 3.0 \times 10^{-4}$, *Nab1* $p = 0.0011$, *Srebp1* $p = 0.0050$, *Mpz* $p = 7.0 \times 10^{-4}$, *Pmp22* p
841 $= 9.0 \times 10^{-4}$, *Mbp* $p = 4.0 \times 10^{-4}$) Schwann cells relative to levels found in *Hgs^{fl}* controls.
842 The level of *Hgs* mRNA was reduced 70% in *P0CreHgs^{fl}* mice relative to controls ($p =$
843 0.0011). Data are shown as mean \pm SEM, $n = 3$ mice per genotype. Student's t-test
844 was used to determine whether there was a significant difference in the means of the
845 datasets.

846

847 Figure 9. Altered expression of the ERBB2/3 pathway in sciatic nerves of HGS-deficient
848 mice. (A) Quantitation of mRNA levels of components in the ERBB pathway in sciatic
849 nerves of P14 *P0CreHgs^{fl}* and *Hgs^{fl}* mice (*ErbB2* $p = 0.51$, *ErbB3* $p = 8.0 \times 10^{-4}$, *Btc* $p =$
850 1.0×10^{-15} , *Nrg1* $p = 5.14 \times 10^{-10}$, *Cd44* $p = 1.0 \times 10^{-15}$, *ErbB4* $p = 1.0 \times 10^{-13}$). Data are
851 shown as mean \pm SEM and are plotted relative to levels found in *Hgs^{fl}* control mice, $n =$
852 3 mice per genotype. Student's t-test was used to determine whether there was a
853 significant difference in the means of the datasets. (B) Representative immunoblots and
854 (C) quantitation of ERBB2 (P7 $p = 0.71$, P14 $p = 0.14$) and (D) pERBB2 normalized to

855 total ERBB2 (P7 $p = 0.0127$, P14 $p = 0.00741$). (E) Representative immunoblots and (F)
856 quantitation of ERBB3 (P7 $p = 0.34$, P14 $p = 0.0034$) and (G) pERBB3 normalized to
857 total ERBB3 (P7 $p = 0.647$, P14 $p = 0.0736$) in sciatic nerve extracts of *Hgs^{fl}* and
858 *P0CreHgs^{fl}* mice. ACTB was used as a loading control. Data are shown as mean \pm
859 SEM, $n = 3$ mice per genotype. (H) Representative immunoblots of the levels of
860 pAKT(T308), pAKT(S473), AKT, pERK, ERK, pNF2 NF2, pGSK3 β and GSK3 β , and (I)
861 quantitation of pAKT(T308) ($p = 0.038$), pAKT(S473) ($p = 0.74$), pERK ($p = 0.55$), pNF2
862 ($p = 0.7925$) and pGSK3 β ($p = 0.1467$) levels in sciatic nerve extracts from P14 *Hgs^{fl}*
863 and *P0CreHgs^{fl}* mice. ACTB was used as a loading control. Data are shown as mean \pm
864 SEM, $n = 4$ mice per genotype. Student's t-test was used to determine whether there
865 was a significant difference in the means of the datasets.

866 |
867 Figure 1-1. Immunoblot of P14 *Hgs^{fl}* and *P0CreHgs^{fl}* sciatic nerves probed with an
868 antibody against the amino-terminus of HGS. An antibody recognizing amino acids 121-
869 173 of HGS was used to probe P14 sciatic nerve extracts.

870
871 Figure 2-1. Open field traces of 4-month-old *Hgs^{fl}* and *P0CreHgs^{fl}* mice. Representative
872 traces of the overall tracking pattern of 4-month-old mice during a 5 min period.

873
874 Figure 7-1. DESeq2 annotated results with normalized counts for P14 sciatic nerves
875 from *Hgs^{fl}* and *P0CreHgs^{fl}* mice.

876

877 Figure 7-2. Gene Ontology Analysis of genes with a fold change $\geq \pm 2$ and q-value $<$
878 0.05 between *Hgs*^{fl} and *P0CreHgs*^{fl} mice showing biological pathways affected by
879 Schwann cell deletion of *Hgs*.

880

881 Figure 7-3. Gene Ontology Analysis of genes with a fold change $\geq \pm 2$ and q-value $<$
882 0.05 between *Hgs*^{fl} and *P0CreHgs*^{fl} mice showing cellular components affected by
883 Schwann cell deletion of *Hgs*.

884

885 Figure 7-4. Gene Ontology Analysis of genes with a fold change $\geq \pm 2$ and q-value $<$
886 0.05 between *Hgs*^{fl} and *P0CreHgs*^{fl} mice showing molecular functions affected by
887 Schwann cell deletion of *Hgs*.

888

889 **References**

- 890 Adams L, Carlson BM, Henderson L, Goldman D (1995) Adaptation of nicotinic
891 acetylcholine receptor, myogenin, and MRF4 gene expression to long-term
892 muscle denervation. *J Cell Biol* 131:1341-1349.
- 893 Alvarez-Prats A, Bjelobaba I, Aldworth Z, Baba T, Abebe D, Kim YJ, Stojilkovic SS,
894 Stopfer M, Balla T (2018) Schwann-Cell-Specific Deletion of Phosphatidylinositol
895 4-Kinase Alpha Causes Aberrant Myelination. *Cell Rep* 23:2881-2890.
- 896 Anders S, Pyl PT, Huber W (2015) HTSeq--a Python framework to work with high-
897 throughput sequencing data. *Bioinformatics* 31:166-169.
- 898 Ang ET, Schafer R, Baltensperger R, Wernig A, Celio M, Oliver SS (2010) Motor axonal
899 sprouting and neuromuscular junction loss in an animal model of Charcot-Marie-
900 Tooth disease. *J Neuropathol Exp Neurol* 69:281-293.
- 901 Arroyo EJ, Birmingham JR, Jr., Rosenfeld MG, Scherer SS (1998) Promyelinating
902 Schwann cells express Tst-1/SCIP/Oct-6. *J Neurosci* 18:7891-7902.
- 903 Azzedine H, Bolino A, Taieb T, Birouk N, Di Duca M, Bouhouche A, Benamou S, Mrabet
904 A, Hammadouche T, Chkili T, Gouider R, Ravazzolo R, Brice A, Laporte J,
905 LeGuern E (2003a) Mutations in MTMR13, a new pseudophosphatase
906 homologue of MTMR2 and Sbf1, in two families with an autosomal recessive
907 demyelinating form of Charcot-Marie-Tooth disease associated with early-onset
908 glaucoma. *Am J Hum Genet* 72:1141-1153.

- 909 Azzedine H, Bolino A, Taieb T, Birouk N, Di Duca M, Bouhouche A, Benamou S, Mrabet
910 A, Hammadouche T, Chkili T, Gouider R, Ravazzolo R, Brice A, Laporte J,
911 LeGuern E (2003b) Mutations in MTMR13, a new pseudophosphatase
912 homologue of MTMR2 and Sbf1, in two families with an autosomal recessive
913 demyelinating form of Charcot-Marie-Tooth disease associated with early-onset
914 glaucoma. *Am J Hum Genet* 72:1141-1153.
- 915 Barisic N, Claeys KG, Sirotkovic-Skerlev M, Lofgren A, Nelis E, De Jonghe P,
916 Timmerman V (2008) Charcot-Marie-Tooth disease: a clinico-genetic
917 confrontation. *Ann Hum Genet* 72:416-441.
- 918 Bean AJ, Davanger S, Chou MF, Gerhardt B, Tsujimoto S, Chang Y (2000) Hrs-2
919 regulates receptor-mediated endocytosis via interactions with Eps15. *J Biol*
920 *Chem* 275:15271-15278.
- 921 Beirowski B, Babetto E, Golden JP, Chen YJ, Yang K, Gross RW, Patti GJ, Milbrandt J
922 (2014a) Metabolic regulator LKB1 is crucial for Schwann cell-mediated axon
923 maintenance. *Nat Neurosci* 17:1351-1361.
- 924 Beirowski B, Babetto E, Golden JP, Chen Y, Yang K, Gross RW, Patti GJ, Milbrandt J
925 (2014b) Metabolic regulator LKB1 is crucial for Schwann cell-mediated axon
926 maintenance. *Nat Neurosci* 17:1351-1361.
- 927 Belleudi F, Leone L, Maggio M, Torrisi MR (2009) Hrs regulates the endocytic sorting of
928 the fibroblast growth factor receptor 2b. *Exp Cell Res* 315:2181-2191.
- 929 Bertelsen V, Stang E (2014) The Mysterious Ways of ErbB2/HER2 Trafficking.
930 *Membranes (Basel)* 4:424-446.
- 931 Berti C, Bartesaghi L, Ghidinelli M, Zambroni D, Figlia G, Chen ZL, Quattrini A, Wrabetz
932 L, Feltri ML (2011) Non-redundant function of dystroglycan and beta1 integrins in
933 radial sorting of axons. *Development* 138:4025-4037.
- 934 Bolino A, Piguat F, Alberizzi V, Pellegatta M, Rivellini C, Guerrero-Valero M, Nosedà R,
935 Brombin C, Nonis A, D'Adamo P, Taveggia C, Previtali SC (2016) Niacin-
936 mediated Tace activation ameliorates CMT neuropathies with focal
937 hypermyelination. *EMBO Mol Med* 8:1438-1454.
- 938 Bolino A, Bolis A, Previtali SC, Dina G, Bussini S, Dati G, Amadio S, Del Carro U, Mruk
939 DD, Feltri ML, Cheng CY, Quattrini A, Wrabetz L (2004) Disruption of Mtmr2
940 produces CMT4B1-like neuropathy with myelin outfolding and impaired
941 spermatogenesis. *J Cell Biol* 167:711-721.
- 942 Bolis A, Zordan P, Coviello S, Bolino A (2007) Myotubularin-related (MTMR)
943 phospholipid phosphatase proteins in the peripheral nervous system. *Mol*
944 *Neurobiol* 35:308-316.
- 945 Bolis A, Coviello S, Bussini S, Dina G, Pardini C, Previtali SC, Malaguti M, Morana P,
946 Del Carro U, Feltri ML, Quattrini A, Wrabetz L, Bolino A (2005) Loss of Mtmr2
947 phosphatase in Schwann cells but not in motor neurons causes Charcot-Marie-
948 Tooth type 4B1 neuropathy with myelin outfoldings. *J Neurosci* 25:8567-8577.
- 949 Brennan KM, Bai Y, Shy ME (2015) Demyelinating CMT--what's known, what's new and
950 what's in store? *Neurosci Lett* 596:14-26.
- 951 Brinkmann BG, Agarwal A, Sereda MW, Garratt AN, Muller T, Wende H, Stassart RM,
952 Nawaz S, Humml C, Velanac V, Radyushkin K, Goebbels S, Fischer TM,
953 Franklin RJ, Lai C, Ehrenreich H, Birchmeier C, Schwab MH, Nave KA (2008)

- 954 Neuregulin-1/ErbB signaling serves distinct functions in myelination of the
955 peripheral and central nervous system. *Neuron* 59:581-595.
- 956 Brown MJ, Asbury AK (1981) Schwann cell proliferation in the postnatal mouse: timing
957 and topography. *Exp Neurol* 74:170-186.
- 958 Cetin H, Beeson D, Vincent A, Webster R (2020) The Structure, Function, and
959 Physiology of the Fetal and Adult Acetylcholine Receptor in Muscle. *Frontiers in*
960 *Molecular Neuroscience* 13.
- 961 Chanut-Delalande H, Jung AC, Baer MM, Lin L, Payre F, Affolter M (2010) The
962 Hrs/Stam complex acts as a positive and negative regulator of RTK signaling
963 during *Drosophila* development. *PLoS One* 5:e10245.
- 964 Chow CY, Zhang Y, Dowling JJ, Jin N, Adamska M, Shiga K, Szigeti K, Shy ME, Li J,
965 Zhang X, Lupski JR, Weisman LS, Meisler MH (2007) Mutation of FIG4 causes
966 neurodegeneration in the pale tremor mouse and patients with CMT4J. *Nature*
967 448:68-72.
- 968 Cipriani S, Phan V, Medard JJ, Horvath R, Lochmuller H, Chrast R, Roos A, Spendiff S
969 (2018) Neuromuscular Junction Changes in a Mouse Model of Charcot-Marie-
970 Tooth Disease Type 4C. *Int J Mol Sci* 19.
- 971 Colby J, Nicholson R, Dickson KM, Orfali W, Naef R, Suter U, Snipes GJ (2000) PMP22
972 carrying the trembler or trembler-J mutation is intracellularly retained in
973 myelinating Schwann cells. *Neurobiol Dis* 7:561-573.
- 974 Cullen PJ, Steinberg F (2018) To degrade or not to degrade: mechanisms and
975 significance of endocytic recycling. *Nat Rev Mol Cell Biol* 19:679-696.
- 976 Dauner K, Eid W, Raghupathy R, Presley JF, Zha X (2017) mTOR complex 1 activity is
977 required to maintain the canonical endocytic recycling pathway against lysosomal
978 delivery. *J Biol Chem* 292:5737-5747.
- 979 Decker L, Desmarquet-Trin-Dinh C, Taillebourg E, Ghislain J, Vallat JM, Charnay P
980 (2006) Peripheral myelin maintenance is a dynamic process requiring constant
981 Krox20 expression. *Journal of Neuroscience* 26:9771-9779.
- 982 Delague V, Jacquier A, Hamadouche T, Poitelon Y, Baudot C, Boccaccio I, Chouery E,
983 Chaouch M, Kassouri N, Jabbour R, Grid D, Megarbane A, Haase G, Levy N
984 (2007) Mutations in FGD4 encoding the Rho GDP/GTP exchange factor FRABIN
985 cause autosomal recessive Charcot-Marie-Tooth type 4H. *Am J Hum Genet*
986 81:1-16.
- 987 Dobin A, Davis CA, Schlesinger F, Drenkow J, Zaleski C, Jha S, Batut P, Chaisson M,
988 Gingeras TR (2013) STAR: ultrafast universal RNA-seq aligner. *Bioinformatics*
989 29:15-21.
- 990 Domenech-Estevez E, Baloui H, Meng X, Zhang Y, Deinhardt K, Dupree JL, Einheber
991 S, Chrast R, Salzer JL (2016) Akt Regulates Axon Wrapping and Myelin Sheath
992 Thickness in the PNS. *J Neurosci* 36:4506-4521.
- 993 Dong C, Palladino SP, Helton ES, Ubogu EE (2016) The pathogenic relevance of
994 alphaM-integrin in Guillain-Barre syndrome. *Acta Neuropathol* 132:739-752.
- 995 Dong C, Greathouse KM, Beacham RL, Palladino SP, Helton ES, Ubogu EE (2017)
996 Fibronectin connecting segment-1 peptide inhibits pathogenic leukocyte
997 trafficking and inflammatory demyelination in experimental models of chronic
998 inflammatory demyelinating polyradiculoneuropathy. *Exp Neurol* 292:35-45.

- 999 Ebner M, Lucic I, Leonard TA, Yudushkin I (2017) PI(3,4,5)P3 Engagement Restricts
1000 Akt Activity to Cellular Membranes. *Mol Cell* 65:416-431 e416.
- 1001 Eiber N, Rehman M, Kravic B, Rudolf R, Sandri M, Hashemolhosseini S (2019) Loss of
1002 Protein Kinase Csnk2b/CK2 beta at Neuromuscular Junctions Affects
1003 Morphology and Dynamics of Aggregated Nicotinic Acetylcholine Receptors,
1004 Neuromuscular Transmission, and Synaptic Gene Expression. *Cells-Basel* 8.
- 1005 Erdem S, Mendell JR, Sahenk Z (1998) Fate of Schwann cells in CMT1A and HNPP:
1006 evidence for apoptosis. *J Neuropathol Exp Neurol* 57:635-642.
- 1007 Evans S, Goldman D, Heinemann S, Patrick J (1987) Muscle acetylcholine receptor
1008 biosynthesis. Regulation by transcript availability. *J Biol Chem* 262:4911-4916.
- 1009 Feltri ML, D'Antonio M, Previtali S, Fasolini M, Messing A, Wrabetz L (1999a) P0-Cre
1010 transgenic mice for inactivation of adhesion molecules in Schwann cells. *Ann N Y*
1011 *Acad Sci* 883:116-123.
- 1012 Feltri ML, D'Antonio M, Previtali S, Fasolini M, Messing A, Wrabetz L (1999b) P0-Cre
1013 transgenic mice for inactivation of adhesion molecules in Schwann cells. *Ann N Y*
1014 *Acad Sci* 883:116-123.
- 1015 Figlia G, Gerber D, Suter U (2018) Myelination and mTOR. *Glia* 66:693-707.
- 1016 Figlia G, Normen C, Pereira JA, Gerber D, Suter U (2017) Dual function of the PI3K-
1017 Akt-mTORC1 axis in myelination of the peripheral nervous system. *Elife* 6.
- 1018 Fledrich R, Stassart RM, Klink A, Rasch LM, Prukop T, Haag L, Czesnik D, Kungl T,
1019 Abdelaal TA, Keric N, Stadelmann C, Bruck W, Nave KA, Sereda MW (2014)
1020 Soluble neuregulin-1 modulates disease pathogenesis in rodent models of
1021 Charcot-Marie-Tooth disease 1A. *Nat Med* 20:1055-1061.
- 1022 Fosdahl AM, Dietrich M, Schink KO, Malik MS, Skeie M, Bertelsen V, Stang E (2017)
1023 ErbB3 interacts with Hrs and is sorted to lysosomes for degradation. *Biochim*
1024 *Biophys Acta* 1864:2241-2252.
- 1025 Garratt AN, Voiculescu O, Topilko P, Charnay P, Birchmeier C (2000) A dual role of
1026 erbB2 in myelination and in expansion of the schwann cell precursor pool. *J Cell*
1027 *Biol* 148:1035-1046.
- 1028 Gerber D, Pereira JA, Gerber J, Tan G, Dimitrieva S, Yanguéz E, Suter U (2021)
1029 Transcriptional profiling of mouse peripheral nerves to the single-cell level to
1030 build a sciatic nerve ATlas (SNAT). *Elife* 10.
- 1031 Goh LK, Sorkin A (2013) Endocytosis of receptor tyrosine kinases. *Cold Spring Harb*
1032 *Perspect Biol* 5:a017459.
- 1033 Goldman D, Brenner HR, Heinemann S (1988) Acetylcholine receptor alpha-, beta-,
1034 gamma-, and delta-subunit mRNA levels are regulated by muscle activity.
1035 *Neuron* 1:329-333.
- 1036 Gomez-Sanchez JA et al. (2015) Schwann cell autophagy, myelinophagy, initiates
1037 myelin clearance from injured nerves. *J Cell Biol* 210:153-168.
- 1038 Grove M, Kim H, Santerre M, Krupka AJ, Han SB, Zhai J, Cho JY, Park R, Harris M,
1039 Kim S, Sawaya BE, Kang SH, Barbe MF, Cho SH, Lemay MA, Son YJ (2017)
1040 YAP/TAZ initiate and maintain Schwann cell myelination. *Elife* 6.
- 1041 Gutmann DH, Haipek CA, Burke SP, Sun CX, Scoles DR, Pulst SM (2001) The NF2
1042 interactor, hepatocyte growth factor-regulated tyrosine kinase substrate (HRS),
1043 associates with merlin in the "open" conformation and suppresses cell growth
1044 and motility. *Hum Mol Genet* 10:825-834.

- 1045 Hahn AF, Chang Y, Webster HD (1987) Development of myelinated nerve fibers in the
1046 sixth cranial nerve of the rat: a quantitative electron microscope study. *J Comp*
1047 *Neurol* 260:491-500.
- 1048 Hanyaloglu AC, McCullagh E, von Zastrow M (2005) Essential role of Hrs in a recycling
1049 mechanism mediating functional resensitization of cell signaling. *Embo J*
1050 24:2265-2283.
- 1051 Haugen LH, Skjeldal FM, Bergeland T, Bakke O (2017) Endosomal binding kinetics of
1052 Eps15 and Hrs specifically regulate the degradation of RTKs. *Sci Rep* 7:17962.
- 1053 Heller BA, Ghidinelli M, Voelkl J, Einheber S, Smith R, Grund E, Morahan G, Chandler
1054 D, Kalaydjieva L, Giancotti F, King RH, Fejes-Toth AN, Fejes-Toth G, Feltri ML,
1055 Lang F, Salzer JL (2014) Functionally distinct PI 3-kinase pathways regulate
1056 myelination in the peripheral nervous system. *J Cell Biol* 204:1219-1236.
- 1057 Hislop JN, Marley A, Von Zastrow M (2004) Role of mammalian vacuolar protein-sorting
1058 proteins in endocytic trafficking of a non-ubiquitinated G protein-coupled receptor
1059 to lysosomes. *J Biol Chem* 279:22522-22531.
- 1060 Horn M, Baumann R, Pereira JA, Sidiropoulos PNM, Somandin C, Welzl H, Stendel C,
1061 Luhmann T, Wessig C, Toyka KV, Relvas JB, Senderek J, Suter U (2012a)
1062 Myelin is dependent on the Charcot-Marie-Tooth Type 4H disease culprit protein
1063 FRABIN/FGD4 in Schwann cells. *Brain* 135:3567-3583.
- 1064 Horn M, Baumann R, Pereira JA, Sidiropoulos PN, Somandin C, Welzl H, Stendel C,
1065 Luhmann T, Wessig C, Toyka KV, Relvas JB, Senderek J, Suter U (2012b)
1066 Myelin is dependent on the Charcot-Marie-Tooth Type 4H disease culprit protein
1067 FRABIN/FGD4 in Schwann cells. *Brain : a journal of neurology* 135:3567-3583.
- 1068 Huang HR, Chen ZJ, Kunes S, Chang GD, Maniatis T (2010) Endocytic pathway is
1069 required for Drosophila Toll innate immune signaling. *Proc Natl Acad Sci U S A*
1070 107:8322-8327.
- 1071 Huang SH, Zhao L, Sun ZP, Li XZ, Geng Z, Zhang KD, Chao MV, Chen ZY (2009)
1072 Essential role of Hrs in endocytic recycling of full-length TrkB receptor but not its
1073 isoform TrkB.T1. *J Biol Chem* 284:15126-15136.
- 1074 Hunter M, Bernard R, Freitas E, Boyer A, Morar B, Martins IJ, Tournev I, Jordanova A,
1075 Guergelcheva V, Ishpekova B, Kremensky I, Nicholson G, Schlotter B,
1076 Lochmuller H, Voit T, Colomer J, Thomas PK, Levy N, Kalaydjieva L (2003)
1077 Mutation screening of the N-myc downstream-regulated gene 1 (NDRG1) in
1078 patients with Charcot-Marie-Tooth Disease. *Hum Mutat* 22:129-135.
- 1079 Hurley JH (2008) ESCRT complexes and the biogenesis of multivesicular bodies. *Curr*
1080 *Opin Cell Biol* 20:4-11.
- 1081 Hurley JH, Emr SD (2006) The ESCRT complexes: structure and mechanism of a
1082 membrane-trafficking network. *Annu Rev Biophys Biomol Struct* 35:277-298.
- 1083 Jessen KR, Mirsky R (2005) The origin and development of glial cells in peripheral
1084 nerves. *Nat Rev Neurosci* 6:671-682.
- 1085 Jessen KR, Mirsky R (2008) Negative regulation of myelination: relevance for
1086 development, injury, and demyelinating disease. *Glia* 56:1552-1565.
- 1087 Jovic M, Sharma M, Rahajeng J, Caplan S (2010) The early endosome: a busy sorting
1088 station for proteins at the crossroads. *Histol Histopathol* 25:99-112.
- 1089 Kachhap SK, Faith D, Qian DZ, Shabbeer S, Galloway NL, Pili R, Denmeade SR,
1090 DeMarzo AM, Carducci MA (2007) The N-Myc down regulated Gene1 (NDRG1)

- 1091 Is a Rab4a effector involved in vesicular recycling of E-cadherin. *PLoS One*
1092 2:e844.
- 1093 Kalaydjieva L, Gresham D, Gooding R, Heather L, Baas F, de Jonge R, Blechschmidt
1094 K, Angelicheva D, Chandler D, Worsley P, Rosenthal A, King RH, Thomas PK
1095 (2000) N-myc downstream-regulated gene 1 is mutated in hereditary motor and
1096 sensory neuropathy-Lom. *Am J Hum Genet* 67:47-58.
- 1097 Kobayashi OH, Tanaka N, Sugamura K (2005) Hrs, a mammalian master molecule in
1098 vesicular transport and protein-sorting, suppresses the degradation of ESCRT
1099 proteins STAM1 and STAM2. *Cell Struct Funct* 30:75-75.
- 1100 Komada M, Soriano P (1999) Hrs, a FYVE finger protein localized to early endosomes,
1101 is implicated in vesicular traffic and required for ventral folding morphogenesis.
1102 *Gene Dev* 13:1475-1485.
- 1103 Komada M, Kitamura N (2005) The Hrs/STAM complex in the downregulation of
1104 receptor tyrosine kinases. *J Biochem* 137:1-8.
- 1105 Kong L, Wang X, Choe DW, Polley M, Burnett BG, Bosch-Marce M, Griffin JW, Rich
1106 MM, Sumner CJ (2009) Impaired synaptic vesicle release and immaturity of
1107 neuromuscular junctions in spinal muscular atrophy mice. *J Neurosci* 29:842-
1108 851.
- 1109 Lee SM, Chin LS, Li L (2012) Charcot-Marie-Tooth disease-linked protein SIMPLE
1110 functions with the ESCRT machinery in endosomal trafficking. *J Cell Biol*
1111 199:799-816.
- 1112 Lee SM, Chin LS, Li L (2016) Dysregulation of ErbB Receptor Trafficking and Signaling
1113 in Demyelinating Charcot-Marie-Tooth Disease. *Mol Neurobiol*.
- 1114 Lee SM, Chin LS, Li L (2017) Dysregulation of ErbB Receptor Trafficking and Signaling
1115 in Demyelinating Charcot-Marie-Tooth Disease. *Molecular Neurobiology* 54:87-
1116 100.
- 1117 Lee SM, Olzmann JA, Chin LS, Li L (2011) Mutations associated with Charcot-Marie-
1118 Tooth disease cause SIMPLE protein mislocalization and degradation by the
1119 proteasome and aggresome-autophagy pathways. *J Cell Sci* 124:3319-3331.
- 1120 Lenferink AE, Pinkas-Kramarski R, van de Poll ML, van Vugt MJ, Klapper LN, Tzahar E,
1121 Waterman H, Sela M, van Zoelen EJ, Yarden Y (1998) Differential endocytic
1122 routing of homo- and hetero-dimeric ErbB tyrosine kinases confers signaling
1123 superiority to receptor heterodimers. *EMBO J* 17:3385-3397.
- 1124 Li W, Zhu H, Zhao X, Brancho D, Liang Y, Zou Y, Bennett C, Chow CW (2015)
1125 Dysregulated Inflammatory Signaling upon Charcot-Marie-Tooth Type 1C
1126 Mutation of SIMPLE Protein. *Mol Cell Biol* 35:2464-2478.
- 1127 Logan AM, Mammel AE, Robinson DC, Chin AL, Condon AF, Robinson FL (2017)
1128 Schwann cell-specific deletion of the endosomal PI 3-kinase Vps34 leads to
1129 delayed radial sorting of axons, arrested myelination, and abnormal ErbB2-ErbB3
1130 tyrosine kinase signaling. *Glia* 65:1452-1470.
- 1131 Love MI, Huber W, Anders S (2014) Moderated estimation of fold change and
1132 dispersion for RNA-seq data with DESeq2. *Genome Biol* 15:550.
- 1133 Lupo V, Galindo MI, Martinez-Rubio D, Sevilla T, Vilchez JJ, Palau F, Espinos C (2009)
1134 Missense mutations in the SH3TC2 protein causing Charcot-Marie-Tooth disease
1135 type 4C affect its localization in the plasma membrane and endocytic pathway.
1136 *Hum Mol Genet* 18:4603-4614.

- 1137 Massa R, Palumbo C, Cavallaro T, Panico MB, Bei R, Terracciano C, Rizzuto N,
1138 Bernardi G, Modesti A (2006) Overexpression of ErbB2 and ErbB3 receptors in
1139 Schwann cells of patients with Charcot-Marie-tooth disease type 1A. *Muscle*
1140 *Nerve* 33:342-349.
- 1141 McNally KE, Cullen PJ (2018) Endosomal Retrieval of Cargo: Retromer Is Not Alone.
1142 *Trends Cell Biol* 28:807-822.
- 1143 Meier H (1967) The neuropathy of teetering, a neurological mutation in the mouse. *Arch*
1144 *Neurol* 16:59-66.
- 1145 Miura S, Mishina Y (2011a) Hepatocyte Growth Factor-Regulated Tyrosine Kinase
1146 Substrate (Hgs) Is Involved in BMP Signaling Through Phosphorylation of
1147 SMADs and TAK1 in Early Mouse Embryo. *Dev Dynam* 240:2474-2481.
- 1148 Miura S, Mishina Y (2011b) Hepatocyte growth factor-regulated tyrosine kinase
1149 substrate (Hgs) is involved in BMP signaling through phosphorylation of smads
1150 and TAK1 in early mouse embryo. *Dev Dyn*.
- 1151 Monje PV, Bunge MB, Wood PM (2006) Cyclic AMP synergistically enhances
1152 neuregulin-dependent ERK and Akt activation and cell cycle progression in
1153 Schwann cells. *Glia* 53:649-659.
- 1154 Monje PV, Athauda G, Wood PM (2008) Protein Kinase A-mediated Gating of
1155 Neuregulin-dependent ErbB2-ErbB3 Activation Underlies the Synergistic Action
1156 of cAMP on Schwann Cell Proliferation. *Journal of Biological Chemistry*
1157 283:34087-34100.
- 1158 Nandini S, Conley Calderon JL, Sabblah TT, Love R, King LE, King SJ (2019) Mice with
1159 an autosomal dominant Charcot-Marie-Tooth type 2O disease mutation in both
1160 dynein alleles display severe moto-sensory phenotypes. *Sci Rep* 9:11979.
- 1161 Naslavsky N, Caplan S (2018) The enigmatic endosome - sorting the ins and outs of
1162 endocytic trafficking. *J Cell Sci* 131.
- 1163 Newbern J, Birchmeier C (2010) Nrg1/ErbB signaling networks in Schwann cell
1164 development and myelination. *Semin Cell Dev Biol* 21:922-928.
- 1165 Newbern JM, Li X, Shoemaker SE, Zhou J, Zhong J, Wu Y, Bonder D, Hollenback S,
1166 Coppola G, Geschwind DH, Landreth GE, Snider WD (2011) Specific functions
1167 for ERK/MAPK signaling during PNS development. *Neuron* 69:91-105.
- 1168 Orita S, Henry K, Mantuano E, Yamauchi K, De Corato A, Ishikawa T, Feltri ML,
1169 Wrabetz L, Gaultier A, Pollack M, Ellisman M, Takahashi K, Gonias SL,
1170 Campana WM (2013) Schwann cell LRP1 regulates remak bundle ultrastructure
1171 and axonal interactions to prevent neuropathic pain. *J Neurosci* 33:5590-5602.
- 1172 Palfy M, Remenyi A, Korcsmaros T (2012) Endosomal crosstalk: meeting points for
1173 signaling pathways. *Trends Cell Biol* 22:447-456.
- 1174 Pereira JA, Lebrun-Julien F, Suter U (2012) Molecular mechanisms regulating
1175 myelination in the peripheral nervous system. *Trends in neurosciences* 35:123-
1176 134.
- 1177 Perkins CS, Aguayo AJ, Bray GM (1981) Schwann cell multiplication in Trembler mice.
1178 *Neuropathol Appl Neurobiol* 7:115-126.
- 1179 Pietiainen V, Vassilev B, Blom T, Wang W, Nelson J, Bittman R, Back N, Zelcer N,
1180 Ikonen E (2013) NDRG1 functions in LDL receptor trafficking by regulating
1181 endosomal recycling and degradation. *J Cell Sci* 126:3961-3971.
- 1182 Pisciotta C, Shy ME (2018) Neuropathy. *Handb Clin Neurol* 148:653-665.

- 1183 Raiborg C, Malerod L, Pedersen NM, Stenmark H (2008) Differential functions of Hrs
1184 and ESCRT proteins in endocytic membrane trafficking. *Exp Cell Res* 314:801-
1185 813.
- 1186 Redpath GMI, Betzler VM, Rossatti P, Rossy J (2020) Membrane Heterogeneity
1187 Controls Cellular Endocytic Trafficking. *Front Cell Dev Biol* 8:757.
- 1188 Riethmacher D, Sonnenberg-Riethmacher E, Brinkmann V, Yamaai T, Lewin GR,
1189 Birchmeier C (1997) Severe neuropathies in mice with targeted mutations in the
1190 ErbB3 receptor. *Nature* 389:725-730.
- 1191 Roberts SL, Dun XP, Doddrell RDS, Mindos T, Drake LK, Onaitis MW, Florio F,
1192 Quattrini A, Lloyd AC, D'Antonio M, Parkinson DB (2017) Sox2 expression in
1193 Schwann cells inhibits myelination in vivo and induces influx of macrophages to
1194 the nerve. *Development* 144:3114-3125.
- 1195 Robinson FL, Niesman IR, Beiswenger KK, Dixon JE (2008) Loss of the inactive
1196 myotubularin-related phosphatase Mtmr13 leads to a Charcot-Marie-Tooth 4B2-
1197 like peripheral neuropathy in mice. *Proc Natl Acad Sci U S A* 105:4916-4921.
- 1198 Rusten TE, Vaccari T, Stenmark H (2011) Shaping development with ESCRTs. *Nat Cell*
1199 *Biol* 14:38-45.
- 1200 Salzer JL (2015) Schwann Cell Myelination. *Cold Spring Harb Perspect Biol* 7.
- 1201 Sancho S, Young P, Suter U (2001) Regulation of Schwann cell proliferation and
1202 apoptosis in PMP22-deficient mice and mouse models of Charcot-Marie-Tooth
1203 disease type 1A. *Brain* 124:2177-2187.
- 1204 Seburn KL, Nangle LA, Cox GA, Schimmel P, Burgess RW (2006) An active dominant
1205 mutation of glycyl-tRNA synthetase causes neuropathy in a Charcot-Marie-Tooth
1206 2D mouse model. *Neuron* 51:715-726.
- 1207 Sidiropoulos PN, Mieke M, Bock T, Tinelli E, Oertli CI, Kuner R, Meijer D, Wollscheid B,
1208 Niemann A, Suter U (2012) Dynamin 2 mutations in Charcot-Marie-Tooth
1209 neuropathy highlight the importance of clathrin-mediated endocytosis in
1210 myelination. *Brain* 135:1395-1411.
- 1211 Sleigh JN, Grice SJ, Burgess RW, Talbot K, Cader MZ (2014) Neuromuscular junction
1212 maturation defects precede impaired lower motor neuron connectivity in Charcot-
1213 Marie-Tooth type 2D mice. *Hum Mol Genet* 23:2639-2650.
- 1214 Sorkin A, Goh LK (2009) Endocytosis and intracellular trafficking of ErbBs. *Exp Cell Res*
1215 315:683-696.
- 1216 Spaulding EL, Sleigh JN, Morelli KH, Pinter MJ, Burgess RW, Seburn KL (2016)
1217 Synaptic Deficits at Neuromuscular Junctions in Two Mouse Models of Charcot-
1218 Marie-Tooth Type 2d. *J Neurosci* 36:3254-3267.
- 1219 Street VA, Bennett CL, Goldy JD, Shirk AJ, Kleopa KA, Tempel BL, Lipe HP, Scherer
1220 SS, Bird TD, Chance PF (2003a) Mutation of a putative protein degradation gene
1221 LITAF/SIMPLE in Charcot-Marie-Tooth disease 1C. *Neurology* 60:22-26.
- 1222 Street VA, Bennett CL, Goldy JD, Shirk AJ, Kleopa KA, Tempel BL, Lipe HP, Scherer
1223 SS, Bird TD, Chance PF (2003b) Mutation of a putative protein degradation gene
1224 LITAF/SIMPLE in Charcot-Marie-Tooth disease 1C. *Neurology* 60:22-26.
- 1225 Sugiyama MG, Fairn GD, Antonescu CN (2019) Akt-ing Up Just About Everywhere:
1226 Compartment-Specific Akt Activation and Function in Receptor Tyrosine Kinase
1227 Signaling. *Frontiers in Cell and Developmental Biology* 7.

- 1228 Sun CX, Haipek C, Scoles DR, Pulst SM, Giovannini M, Komada M, Gutmann DH
1229 (2002) Functional analysis of the relationship between the neurofibromatosis 2
1230 tumor suppressor and its binding partner, hepatocyte growth factor-regulated
1231 tyrosine kinase substrate. *Hum Mol Genet* 11:3167-3178.
- 1232 Syed N, Reddy K, Yang DP, Taveggia C, Salzer JL, Maurel P, Kim HA (2010) Soluble
1233 neuregulin-1 has bifunctional, concentration-dependent effects on Schwann cell
1234 myelination. *J Neurosci* 30:6122-6131.
- 1235 Topilko P, Schneider-Maunoury S, Levi G, Baron-Van Evercooren A, Chennoufi AB,
1236 Seitanidou T, Babinet C, Charnay P (1994) Krox-20 controls myelination in the
1237 peripheral nervous system. *Nature* 371:796-799.
- 1238 Ubogu EE, Yosef N, Xia RH, Sheikh KA (2012) Behavioral, electrophysiological, and
1239 histopathological characterization of a severe murine chronic demyelinating
1240 polyneuritis model. *J Peripher Nerv Syst* 17:53-61.
- 1241 Vaden JH, Bhattacharyya BJ, Chen PC, Watson JA, Marshall AG, Phillips SE, Wilson
1242 JA, King GD, Miller RJ, Wilson SM (2015) Ubiquitin-specific protease 14
1243 regulates c-Jun N-terminal kinase signaling at the neuromuscular junction.
1244 *Molecular neurodegeneration* 10:3.
- 1245 Villasenor R, Kalaidzidis Y, Zerial M (2016) Signal processing by the endosomal
1246 system. *Curr Opin Cell Biol* 39:53-60.
- 1247 Watson JA, Bhattacharyya BJ, Vaden JH, Wilson JA, Icyuz M, Howard AD, Phillips E,
1248 DeSilva TM, Siegal GP, Bean AJ, King GD, Phillips SE, Miller RJ, Wilson SM
1249 (2015a) Motor and Sensory Deficits in the teetering Mice Result from Mutation of
1250 the ESCRT Component HGS. *PLoS Genet* 11:e1005290.
- 1251 Watson JA, Bhattacharyya BJ, Vaden JH, Wilson JA, Icyuz M, Howard AD, Phillips E,
1252 DeSilva TM, Siegal GP, Bean AJ, King GD, Phillips SE, Miller RJ, Wilson SM
1253 (2015b) Motor and Sensory Deficits in the teetering Mice Result from Mutation of
1254 the ESCRT Component HGS. *Plos Genet* 11.
- 1255 Witzemann V (1989) Control of acetylcholine receptors in skeletal muscle. *J Protein*
1256 *Chem* 8:333-335.
- 1257 Yan Q, Sun W, Kujala P, Lotfi Y, Vida TA, Bean AJ (2005) CART: an Hrs/actinin-
1258 4/BERP/myosin V protein complex required for efficient receptor recycling. *Mol*
1259 *Biol Cell* 16:2470-2482.
- 1260 Yin X, Kidd GJ, Pioro EP, McDonough J, Dutta R, Feltri ML, Wrabetz L, Messing A,
1261 Wyatt RM, Balice-Gordon RJ, Trapp BD (2004) Dysmyelinated lower motor
1262 neurons retract and regenerate dysfunctional synaptic terminals. *J Neurosci*
1263 24:3890-3898.
- 1264 Zoidl G, Blass-Kampmann S, D'Urso D, Schmalenbach C, Muller HW (1995) Retroviral-
1265 mediated gene transfer of the peripheral myelin protein PMP22 in Schwann cells:
1266 modulation of cell growth. *Embo J* 14:1122-1128.
- 1267

Figure 1

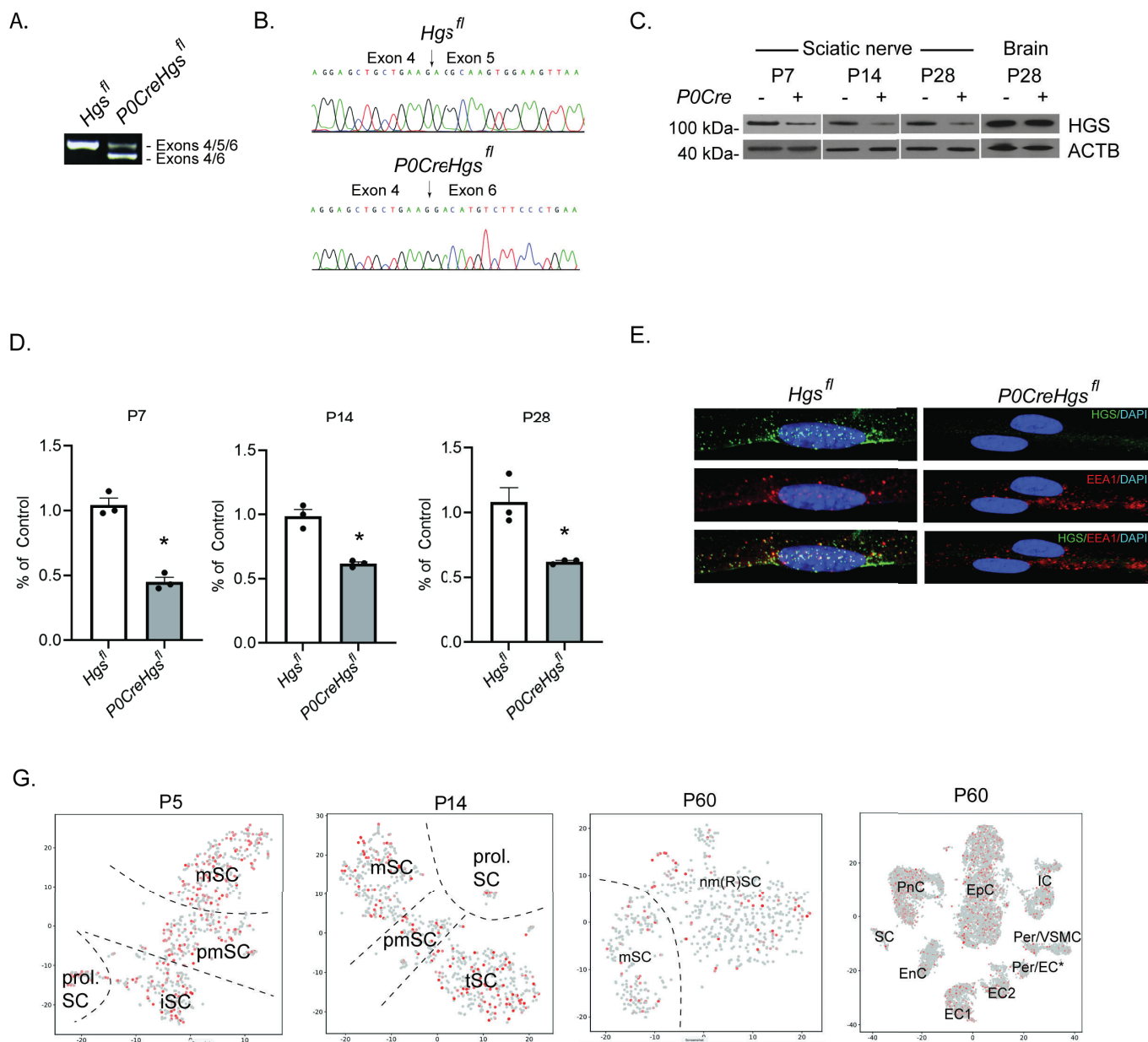


Figure 2

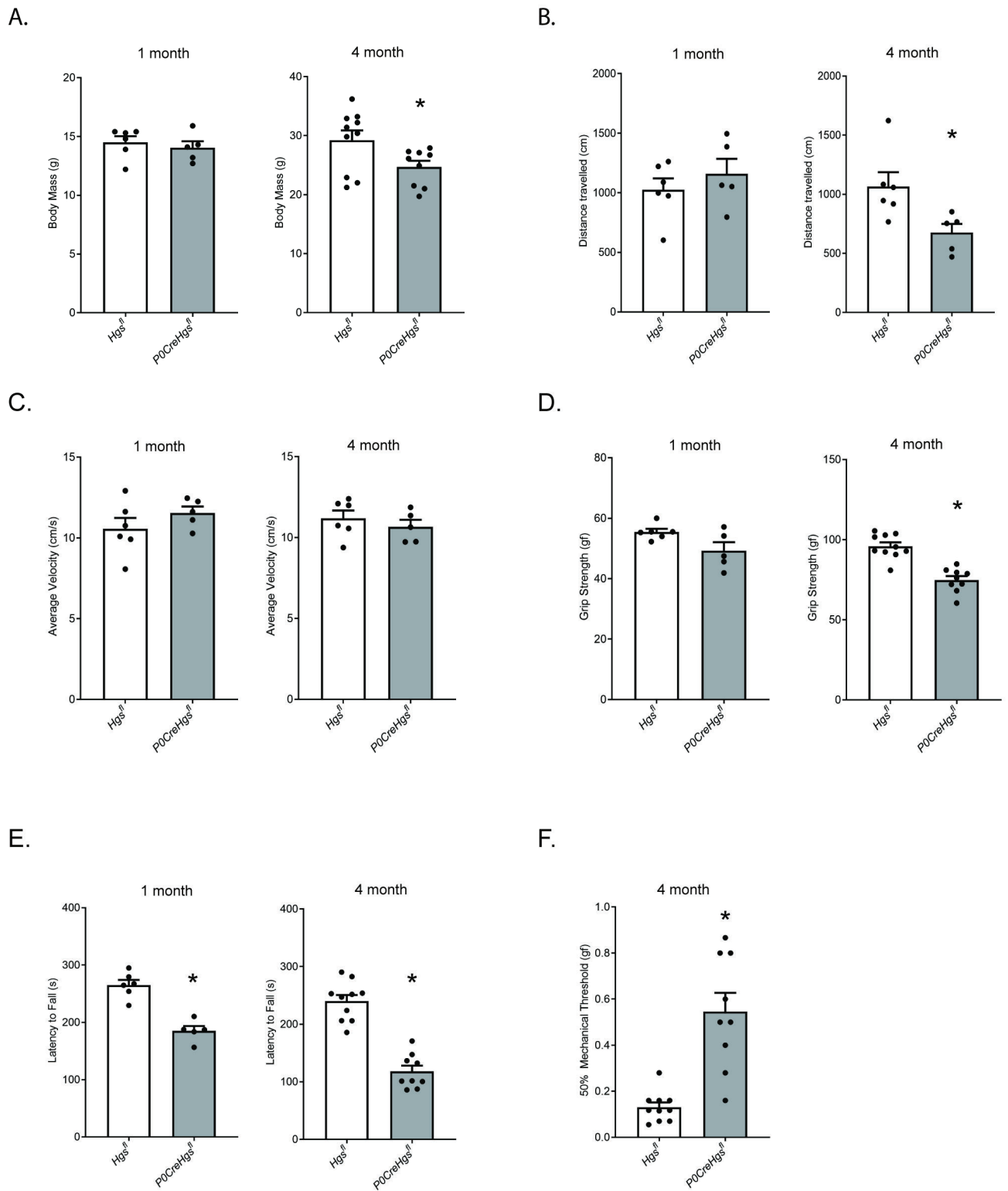


Figure 3

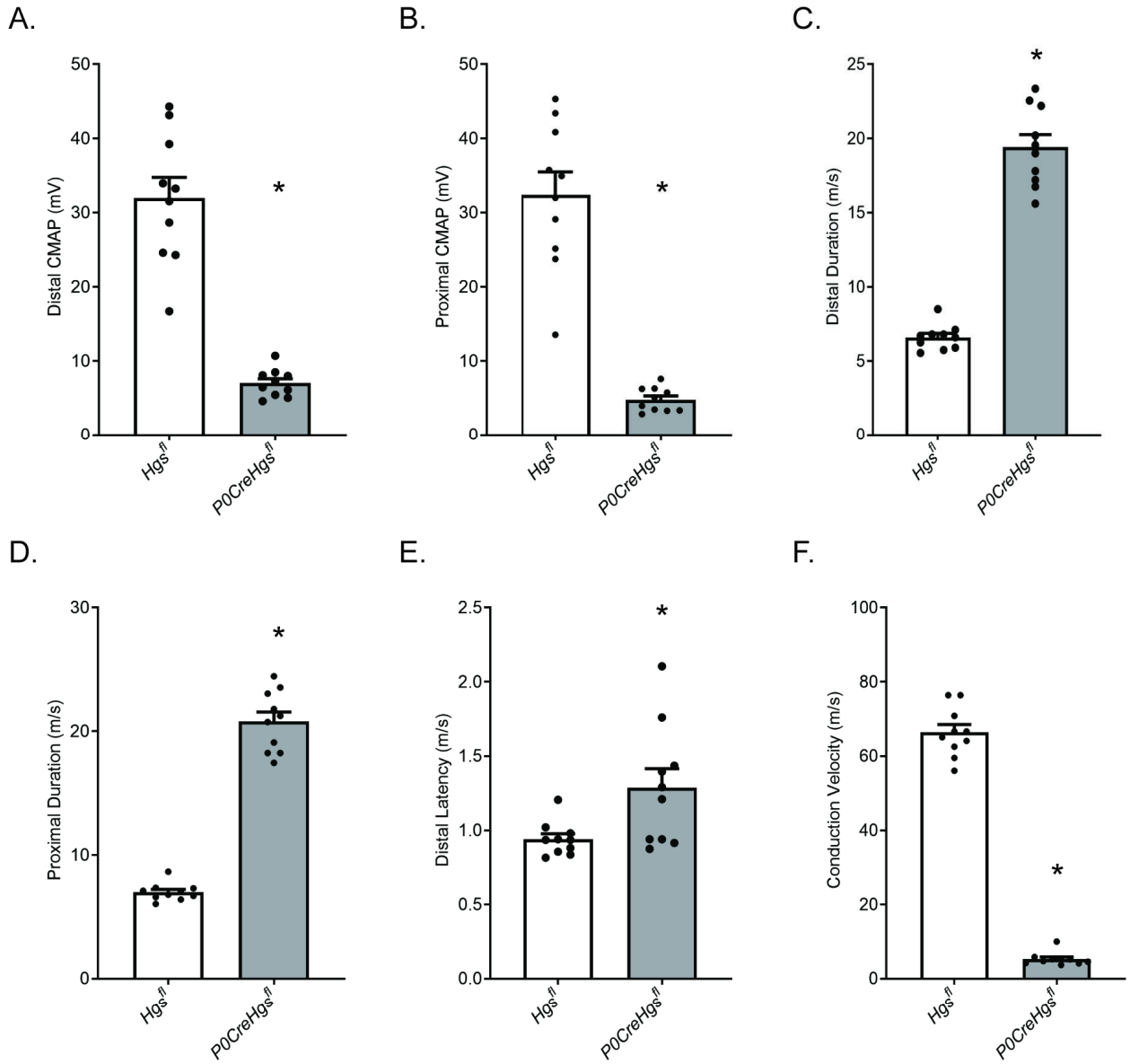


Figure 4

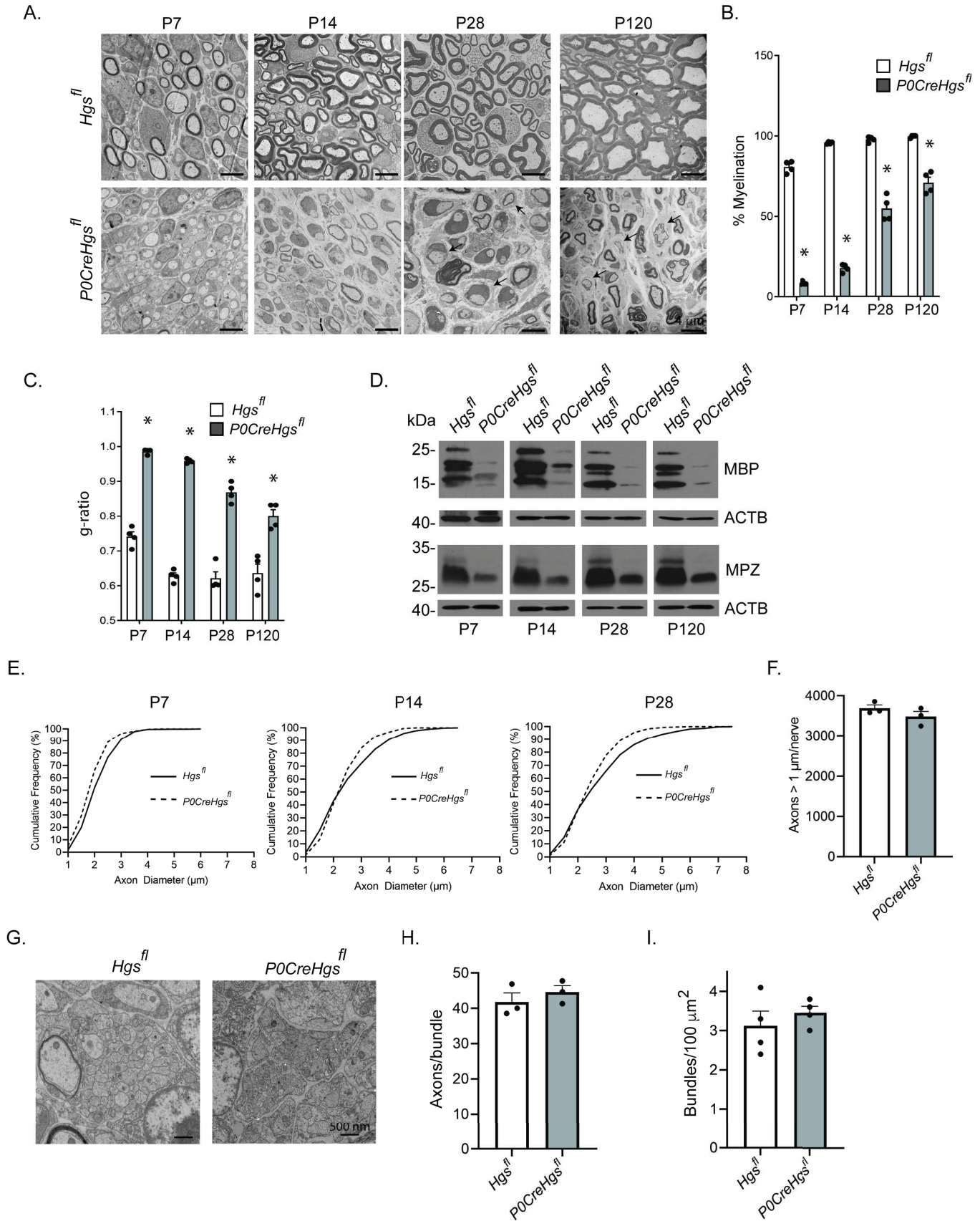


Figure 5

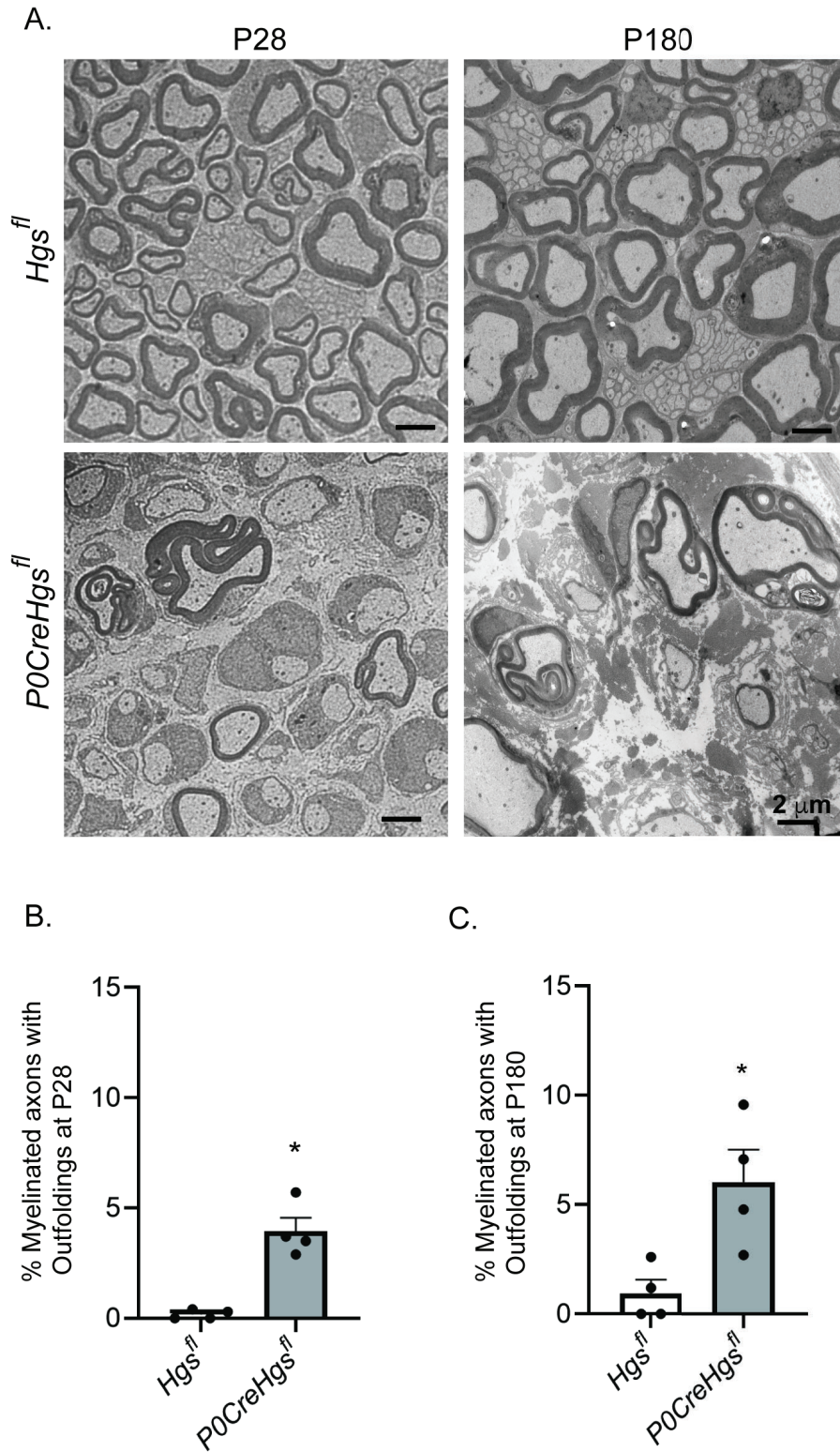


Figure 6

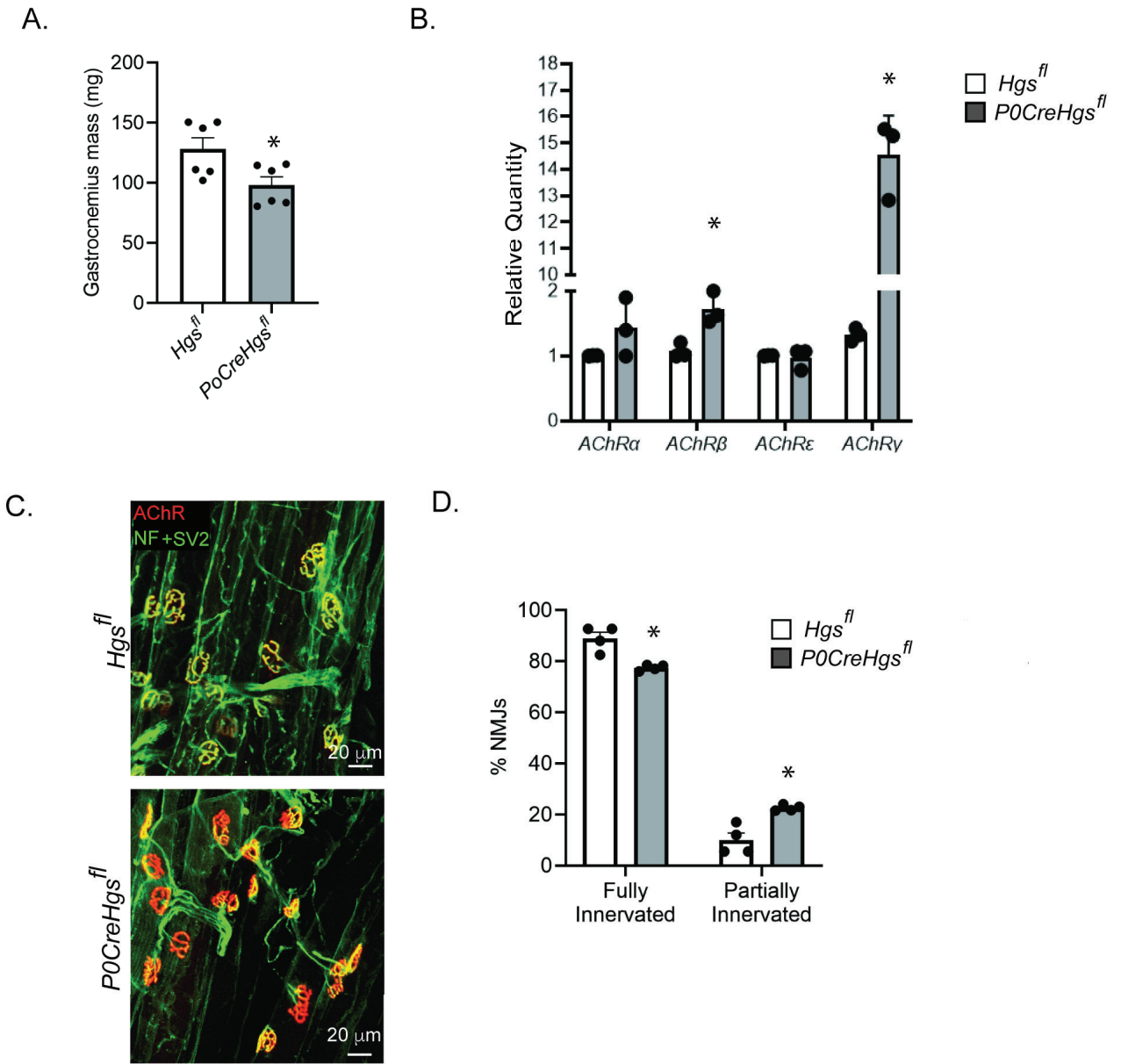


Figure 7

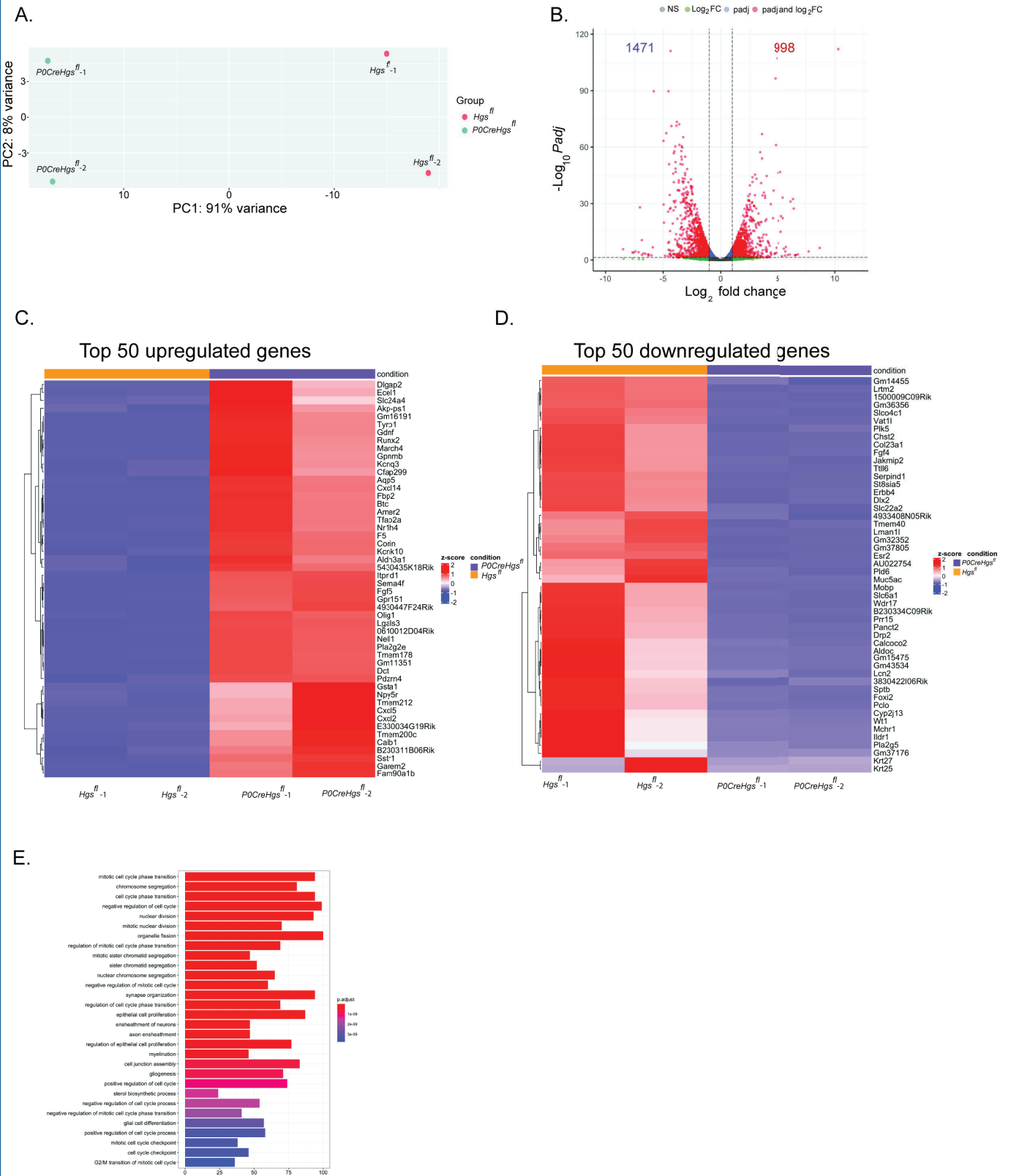


Figure 8

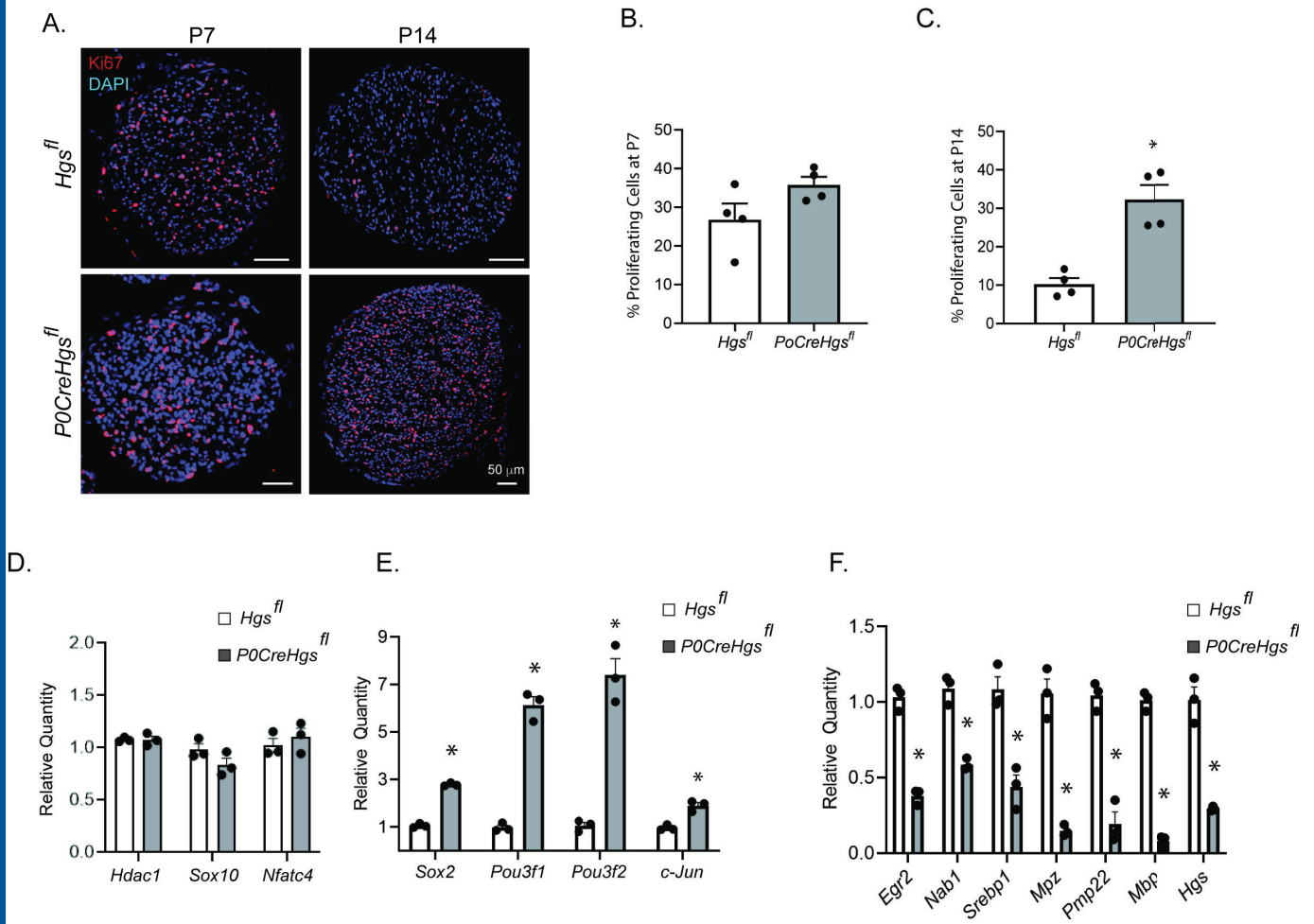


Figure 9

